Review

Oliver Janka, Oliver Niehaus, Rainer Pöttgen* and Bernard Chevalier

Cerium intermetallics with TiNiSi-type structure

DOI 10.1515/znb-2016-0101
Received April 29, 2016; accepted May 11, 2016

Abstract: Intermetallic compounds with the equiatomic composition Ce*TX* that crystallize with the orthorhombic TiNiSi-type structure can be synthesized with electron-rich transition metals (*T*) and *X* = Zn, Al, Ga, Si, Ge, Sn, As, Sb, and Bi. The present review focusses on the crystal chemistry and chemical bonding of these Ce*TX* phases and on their physical properties, ^{119}Sn and ^{121}Sb Mössbauer spectra, high-pressure effects, hydrogenation reactions and the formation of solid solutions in order to elucidate structure–property relationships. This paper is the final one of a series of four reviews on equiatomic intermetallic cerium compounds [Part I: *Z. Naturforsch*. **2015**, *70b*, 289; Part II: *Z. Naturforsch*. **2015**, *70b*, 695; Part III: *Z. Naturforsch*. **2016**, *71b*, 165].

Keywords: cerium compounds; crystal structure; intermetallics; physical properties; structure–property relationship.

1 Introduction

Among the huge number of rare earth (RE) based intermetallic compounds [1] those of cerium have broadly been studied in the context of strongly correlated electron systems [2–7]. The large variations of the magnetic and electrical properties of such cerium intermetallics result from the possibility of cerium to adopt two different valence states, diamagnetic Ce^{4+} with [Xe] configuration, paramagnetic Ce^{3+} with [Xe]$4f^1$ configuration, or an intermediate valence, leading to Kondo compounds, antiferromagnetic and ferromagnetic ordering, valence fluctuation, heavy fermion properties, superconductivity, or non-Fermi liquid behavior.

The equiatomic Ce*TX* compounds (*T* = electron-rich transition metal; *X* = element of the 3rd, 4th, or 5th main group) form the largest family of cerium intermetallics as they have large flexibility through substitution on both the *T* and *X* sites. A manifold of phases has thoroughly been studied with respect to structural and physical properties over the last 30 years. Some overviews are given in references [2, 8, 9]. While keeping the equiatomic composition, the Ce*TX* phases show changes in their crystal structure, although most of them adopt the hexagonal ZrNiAl [10–12] or the orthorhombic TiNiSi [13] type.

We started to systematically review the synthesis condition, the crystal chemistry, the chemical bonding, and the physical properties of the impressive series of equiatomic Ce*TX* phases. We have organized this large field into three parts. Our first review focused on the Ce*TX* phases with hexagonal ZrNiAl-type structure [14] and herein we summarize the phases with the orthorhombic TiNiSi type. Also those phases that have been assigned the $CeCu_2/KHg_2$ type (the subcell structure of the TiNiSi type) with a statistical *T*/*X* occupancy are included.

2 Synthesis conditions

Starting materials for the synthesis of the Ce*TX* compounds are always the pure elements. The synthesis conditions for the Ce*TX* phases mainly depend on the boiling temperature of the *X* element used. In the case of a high boiling temperature the samples can be prepared by arc-melting [15] under purified argon. Re-melting the samples several times ensures homogeneity. Mostly the product samples are further annealed for longer periods (up to several weeks) in sealed silica ampoules in tube or muffle furnaces. The annealing temperatures vary between 870 and 1270 K. For details we refer to the original articles. The samples are often quenched after the annealing sequences. However, for the growth of small crystals for structure determination slow cooling rates (down to 1 K per hour) are desirable. This is easily possible though

***Corresponding author: Rainer Pöttgen,** Institut für Anorganische und Analytische Chemie, Universität Münster, Corrensstrasse 30, 48149 Münster, Germany, e-mail: pottgen@uni-muenster.de
Oliver Janka and Oliver Niehaus: Institut für Anorganische und Analytische Chemie, Universität Münster, Corrensstrasse 30, 48149 Münster, Germany
Bernard Chevalier: Institut de Chimie de la Matière Condensée de Bordeaux (ICMCB), CNRS [UPR 9048], Université de Bordeaux, Avenue du Docteur A. Schweitzer, 33608 Pessac Cedex, France

programmable power supplies. Arc-melting is used also to obtain large samples for neutron diffraction experiments; e.g. Kitazawa et al. prepared 25 g quantities of CePtAl [16]. Arc-melting was also employed for the preparation of CeRhBi. Salamakha et al. used an excess of bismuth to compensate the loss through evaporation [17]. Alternatively one can react a RhBi precursor with an appropriate amount of cerium metal [18].

As arc-melting proceeds in open, water-cooled crucibles [19], evaporation of elements with low boiling points leads to significant losses. In the case of the TiNiSi-type Ce*TX* compounds reviewed herein, this applies to magnesium, zinc, arsenic, antimony, and bismuth. Addition of an excess of these elements indeed helps for the formation of the phases, but purity of the material cannot be guaranteed. A striking example is the synthesis of CePtZn [20, 21], where zinc already boils (1180 K) before platinum melts (2045 K) [22].

Much better results were obtained through reactions in sealed high-melting metal tubes. The inert transition metals niobium, tantalum and molybdenum were used as crucible materials [23]. The metal containers are usually inductively heated in special water-cooled sample chambers under flowing argon [24, 25], or under secondary vacuum. The latter technique was used for CeMgSn [26, 27], CeAgGa and CeAuGa [28] and the stannide CePdSn [29].

An alternative technique to arc-melting is cold crucible levitation melting. Different experimental setups can easily be found by a standard internet search. This technique was used for the synthesis of the germanides Ce*T*Ge (*T* = Rh, Pd, Ir, Pt) [30].

Although most physical property studies on the Ce*TX* phases were performed on polycrystalline samples, single crystals are required for (i) precise refinements of the structures and (ii) for orientation dependent physical property measurements. For structure refinement one needs only μm-sized specimens. Such small crystals can often directly be separated from long-term annealed samples by mechanical fragmentation. Better crystal quality can be obtained by an additional annealing process in an induction furnace, presented for CePdGe [31] and also applied to CeIrSb [32].

The growth of larger crystals in the mm to cm scale proceeds through the standard crystal growth techniques. High-quality crystals of CePtAl were grown with the Czochralski pulling method using tri- or tetra-arc furnaces [33, 34]. The Bridgman technique was used for the growth of CeRhAs and CeRhSb crystals [17, 35, 36]. For CeRhAs elemental arsenic and a pre-melted ingot of composition $CeRh_{1.02}$ were used as starting materials and molybdenum was taken as crucible material. After an initial heating step (to 1920 K), slow cooling of the crucible led to crystal growth with lump sizes around 3 mm. The same technique was used for CeRhBi [18].

Few high-pressure high-temperature experiments were conducted for the orthorhombic Ce*TX* phases. The stannides Ce*T*Sn (*T* = Ni, Pd, Pt) [37–39] were treated in a multianvil assembly [40–43] using boron nitride as inner crucible material. The arc-melted and carefully ground normal-pressure phases were loaded into the assemblies and treated under maximum pressure and temperature conditions of 11.5 GPa and 1470 K. CeAuGe [44] was treated under hydrostatic pressure in a diamond anvil cell [45] to study structural distortions.

Several TiNiSi-type Ce*TX* phases have thoroughly been thoroughly studied with respect to their hydrogenation behavior in order to probe modifications of the physical properties. General overviews on the samples and experimental conditions are given in [46–49]. Compact arc-melted Ce*TX* phases were used as starting phases for hydrogenation. Mostly the samples were activated under vacuum at higher temperature prior to hydrogen uptake (desorption of volatile surface impurities).

Subsequent hydrogenation proceeds either at room temperature or at slightly elevated temperature with hydrogen pressures up to ca. 45 bar. Cycling of the hydride ensures the homogeneity of the sample. The absorbed hydrogen quantity can be estimated from pressure changes in a calibrated volume. During the hydrogenation reaction the samples crumble completely. For neutron diffraction studies hydrogen is replaced by deuterium. An important parameter concerns the kinetics of hydrogen absorption which can be monitored through absorption isotherms. Although the samples were pre-activated (*vide ultra*), additional surface passivation leads to slow initial hydrogen uptake. The detailed experimental hydrogenation parameters are documented in the original papers.

3 Discussion

3.1 Crystal chemistry and chemical bonding

More than 30 intermetallic cerium compounds Ce*TX* crystallize with the orthorhombic TiNiSi-type structure [13], space group *Pnma*, Pearson symbol oP12, and Wyckoff sequence c^3. The basic crystallographic data of these phases are listed in Table 1. The TiNiSi-type structure is one of the basic structure types for equiatomic alkaline earth, RE, and actinoid intermetallics with more than

Table 1: Lattice parameters and magnetic behavior of CeMg*X* and Ce*TX* phases with orthorhombic TiNiSi-type structure.

Compound	*a*/pm	*b*/pm	*c*/pm	*V*/nm³	Magnetic behavior	Reference
p element compounds						
CeMgSn	772.71(2)	464.80(1)	908.18(2)	0.3262	n.i.	[50]
CeMgSn	773.0(2)	464.9(1)	908.6(2)	0.3266	n.i.	[27]
CeMgSn	773.1(1)	464.9(1)	908.3(1)	0.3264	T_N = 12 K	[26]
d element compounds						
CeCuZn[a]	454.1(1)	722.9(2)	758.1(2)	0.2489	n.i.	[51]
β-CePdZn	707.2(2)	441.4(2)	806.3(3)	0.2517	T_N = 3.2 K	[52]
CeAgZn[a]	472.2(2)	719.1(8)	803.4(5)	0.2728	n.i.	[51]
CePtZn	706.89(19)	435.08(15)	809.71(16)	0.2490	<2 K	[20]
CePtZn	707.4(2)	436.0(1)	810.4(1)	0.2499	T_N = 1.7 K	[21]
CeAuZn	719.2(2)	462.7(1)	796.5(2)	0.2651	<2.1 K	[65]
CeAuZn	722.9	460.7	796.3	0.2674	T_N = 1.7 K	[117]
CeZnAl[a]	463.4(2)	761.0(2)	773.5(5)	0.2728	n.i.	[53]
CeAgAl[a]	470.6	751.6	794.2	0.2809	T_C = 2.9 K	[54]
CeAgAl[a]	470.6(1)	751.6(2)	794.2(2)	0.2809	n.i.	[51]
CeAgAl[a]	470	751	795	0.2806	<1.6 K	[116]
CeIrAl	689.31(4)	432.05(2)	793.61(4)	0.2364	IV	[55]
CeIrAl	689.54	432.11	794.11	0.2366	n.i.	[56]
CeIrAl	689.6	431.6	794.3	0.2364	IV	[57]
CePtAl	719.98(6)	448.17(4)	779.38(5)	0.2515	T_C = 6.5 K	[58]
CePtAl	720.5(4)	447.1(2)	778.0(5)	0.2513	n.i.	[59]
CePtAl	720.8(5)	448.1(5)	774.0(5)	0.2500	T_C = 5.8 K	[60]
CePtAl	720.1	448.2	779.4	0.2516	T_C = 8 K	[109]
CePtAl	720.84(15)	448.91(9)	771.90(17)	0.2498	T_C = 5.9 K	[16]
CeAuAl	757.56(7)	458.77(3)	772.15(6)	0.2684	IV	[61]
CeAuAl	756.2(6)	458.9(3)	772.7(4)	0.2681	T_N = 3.8 K	[62]
CeAuAl	758.6	459	771.4	0.2686	n.i.	[109]
HT-CeNiGa	744.77(15)	453.08(9)	679.23(14)	0.2292	IV	[63]
CeCuGa[a]	451.8	744.9	753.0	0.2534	n.i.	[64]
CeCuGa[a]	449.7	741.2	751.8	0.2506	HF	[114]
CeRhGa	685.1(3)	437.26(16)	784.6(3)	0.2350	IV	[66]
CeRhGa	688.2(2)	439.6(1)	788.9(1)	0.2387	IV	[67]
CeRhGa	685.59(8)	437.73(4)	785.70(7)	0.2358	IV	[68]
CePdGa	719.5(3)	455.3(1)	772.4(2)	0.2530	n.i.	[69]
CeAgGa[a]	465.8	744.3	791.8	0.2745	n.i.	[28]
CeAgGa[a]	467.66(9)	741.36(13)	794.36(15)	0.2754	T_f = 5.1 K	[70]
CeAgGa[a]	467.80(7)	739.3(1)	793.2(1)	0.2743	n.i.	[115]
CeIrGa	690.1(1)	436.6(1)	785.2(2)	0.2366	n.i.	[67]
CeIrGa	702.6(3)	438.29(12)	782.11(13)	0.2408	T_N = 9 K	[68]
CeIrGa	689.3(1)	436.3(1)	783.5(1)	0.2356	IV	[71]
CePtGa	715.7(2)	448.7(1)	776.8(2)	0.2495	n.i.	[69]
CePtGa	715.9(2)	449.1(2)	775.9(3)	0.2494	T_N = 3.4 K	[112]
CePtGa	716.91	449.51	777.15	0.2504	T_N = 3.5 K	[113]
CeAuGa[a]	459.5	742.0	788.1	0.2687	n.i.	[28]
CeRuSi	710.5(4)	425.6(2)	730.1(3)	0.2208	n.i.	[72]
CeNiGe	724.18(3)	430.78(2)	724.08(4)	0.2259	n.i.	[73]
CeNiGe	724.69(5)	430.83(3)	723.79(6)	0.2260	IV	[74]
CePdGe[a]	448.75(7)	730.0(3)	767.6(3)	0.2515	T_N = 3.4 K	[30]
CePdGe[a]	448.73(9)	730.5(1)	767.9(2)	0.2517	n.i.	[69]
CePdGe[a]	448.75	730.01	767.59	0.2515	n.i.	[75]
CePdGe	2190.2(9)	448.4(2)	767.3(3)	0.7535	n.i.	[31]
CeRhGe	743.0(4)	446.6(2)	712.0(4)	0.2362	T_N = 10.5 K	[30]
CeRhGe	742.4(2)	446.8(2)	712.0(3)	0.2362	n.i.	[69]
CeRhGe	742.9(2)	446.7(2)	712.1(2)	0.2363	n.i.	[76]
HT-CeRhGe	724.579(6)	447.506(4)	743.579(6)	0.2411	n.i.	[77]
CeIrGe	707.3(3)	437.40(4)	757.48(18)	0.2343	IV	[30]
CeIrGe	707.1(1)	437.5(1)	757.4(1)	0.2343	n.i.	[69]

Table 1 (continued)

Compound	*a*/pm	*b*/pm	*c*/pm	*V*/nm³	Magnetic behavior	Reference
CeIrGe	707.2(1)	437.42(7)	757.3(1)	0.2343	n.i.	[76]
CePtGe[a]	445.15(8)	734.4(2)	761.6(4)	0.2490	T_N = 3.4 K	[30]
CePtGe[a]	445.0(1)	734.7(3)	761.5(3)	0.2490	n.i.	[69]
CePtGe[a]	444.5(2)	732.9(3)	760.9(3)	0.2479	n.i.	[78]
CePtGe	445.0(1)	1464.8(3)	761.8(2)	0.4966	T_N = 4 K	[110]
HP-CeAuGe	715.9(1)	438.42(9)	767.4(2)	0.2409	n.i.	[45]
CeNiSn	753.7(3)	459.6(1)	761.5(2)	0.2638	n.i.	[37]
CeNiSn	752.3(3)	459.2(2)	756.1(5)	0.2612	n.i.	[79]
CeNiSn	753.91(1)	459.73(1)	763.01(1)	0.2645	n.i.	[47]
CeNiSn	754.0	460.2	761.4	0.2642	IV	[80]
CeNiSn	754.2(1)	460.1(1)	761.7(1)	0.2643	n.i.	[81]
CeNiSn	754(1)	459.9(6)	763.9(9)	0.2649	n.i.	[82]
CeNiSn	754.2(1)	460.09(4)	761.7(1)	0.2643	n.i.	[83]
CePdSn	754.1(2)	470.6(1)	798.4(3)	0.2833	n.i.	[38]
CePdSn	753.0(2)	469.8(1)	795.7(2)	0.2815	T_N = 7.2 K	[49]
CePdSn	752.6	474.2	793.1	0.2830	T_N = 7.5 K	[84]
CePdSn	753.5	470.0	795.5	0.2817	n.i.	[85]
CePdSn	754.1	470.5	798.4	0.2833	n.i.	[29]
CePdSn	752.7(3)	474.5(2)	794.6(3)	0.2838	T_N = 6 K	[86]
CePdSn	753.56(9)	470.45(4)	796.48(9)	0.2824	n.i.	[83]
CePtSn	746.89(9)	462.88(4)	801.93(7)	0.2772	n.i.	[39]
CePtSn	746.3(1)	462.83(6)	801.59(8)	0.2769	n.i.	[83]
CeRhAs	753.51(9)	430.81(6)	736.53(9)	0.2391	n.i.	[17]
CeRhSb	742.0	461.9	785.9	0.2694	IV	[87]
CeRhSb	740.8(1)	460.5(1)	786.1(2)	0.2682	n.i.	[88]
CeRhSb	741.50(3)	461.85(2)	785.70(3)	0.2691	n.i.	[17]
CeRhSb	741.58(9)	461.80(9)	785.77(8)	0.2691	IV	[89]
CeIrSb	736.0(1)	457.8(1)	793.1(2)	0.2672	n.i.	[88]
CeIrSb	733.5(1)	457.03(5)	791.6(1)	0.2654	IV	[32]
CeRhBi	746.48(5)	471.73(4)	797.15(6)	0.2807	n.i.	[17]
CeRhBi	743.8	474.0	798.5	0.2815	<2 K	[18]

IV, Intermediate valence; T_N, Néel temperature; T_C, Curie temperature; T_f, spin freezing temperature; HF, heavy fermion; n.i., not investigated. For samples that did not show magnetic ordering the lowest measuring temperature is given. [a]Only the KHg_2-type subcell data were reported. For details see the chapter *Crystal Chemistry*.

1500 representatives listed in the Pearson data base [1]. As an example for the whole series of Ce*TX* compounds we focus on CeRhGe [76, 77] for the following crystal chemical discussion.

The CeRhGe structure is derived from the well-known hexagonal aristotype AlB_2. The corresponding group-subgroup relation in the Bärnighausen formalism [90–93] is presented in Fig. 1. Generally spoken, the TiNiSi-type phases are strongly orthorhombically distorted ordering variants of AlB_2. In the first step of the symmetry reduction the space group symmetry is reduced from *P*6/*mmm* to *Cmmm* (orthohexagonal setting) through a *translationengleiche* symmetry reduction of index 3 (t3). The second step is a *klassengleiche* transition of index 2 (k2) to space group *Imma* along with a doubling of the unit cell. The representative structure type for this space group symmetry is KHg_2 [94]. The symmetry reduction allows a decoupling of the unit cell parameters and strong tilting of the honey-comb network which is planar in the aristotype AlB_2 as well as in the *Cmmm* setting.

The KHg_2 type, however, does not allow for an ordering of the *T* and *X* atoms, since the mercury atoms are all on Wyckoff site 8*h*. Nevertheless, several Ce*TX* phases have been ascribed to the KHg_2 type with a random 50/50 occupancy of the *T* and *X* atoms on the 8*h* site. As an example we list CeAuGa [28] in the Bärnighausen tree (Fig. 1). Keeping the largely differing chemical potentials of the *T* and *X* atoms in mind, the statistical occupancy is energetically disfavored, but several of these disordered phases exist. The *T*/*X* disorder has a drastic effect on the physical properties, disturbing the Ce(4f)-*T*(*n*d) hybridization and thus the magnetic long-range ordering. Such compounds show inhomogeneous magnetic ground states leading to mictomagnetism/spin glass behavior. A typical example

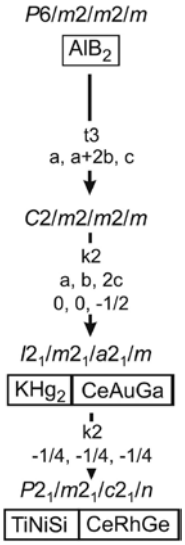

Fig. 1: Group-subgroup sheme in the Bärnighausen formalism [90–93] for AlB_2, KHg_2 (CeAuGa) and TiNiSi (CeRhGe). The indices for the *translationengleiche* (t) and *klassengleiche* (k) symmetry reductions, and the unit cell transformations are given. *Imam* and *Pmcn* are non-standard settings of *Imma* and *Pnma*.

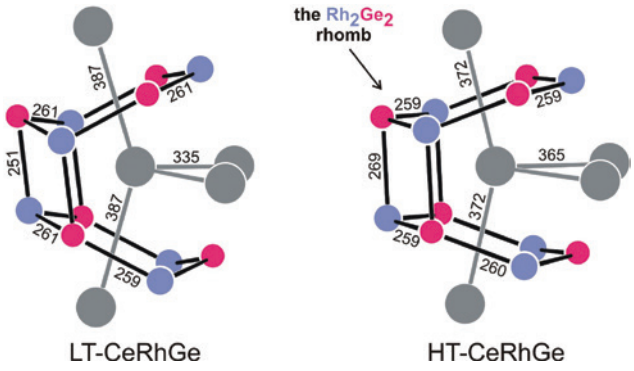

Fig. 2: Coordination of the cerium atoms in the low- and high-temperature modification of CeRhGe. Cerium, rhodium, and germanium atoms are drawn as medium gray, blue, and magenta circles, respectively. Relevant interatomic distances (pm) and the Rh_2Ge_2 rhombs are emphasized.

in the series of Ce*TX* intermetallics is CeAgAl [54]. Such a disorder can also occur if the *T* and *X* atoms are very close in their radii.

Complete *T*/*X* ordering deserves a further symmetry reduction. This is a *klassengleiche* step of index 2 (k2) from *Imma* to *Pnma* (the non-standard settings *Imam* and *Pmcn* were used in Fig. 1 one in order to avoid non-cyclic cell transformations). This decentering of the lattice leads to superstructure reflections (so-called *primitive reflections*). In the cases of *T*/*X* pairs with comparable scattering power the superstructure reflections can be weak and easily be missed in X-ray powder patterns. For an exhaustive overview on AlB_2 related superstructures discussed on the basis of group-subgroup schemes we refer to [95, 96].

The cerium near-neighbor coordinations in the low- and high-temperature modifications of CeRhGe (a first-order structural phase transition occurs around 520 K) [77] are presented in Fig. 2. Each cerium atom is coordinated by two strongly tilted and orthorhombically distorted Rh_3Ge_3 hexagons. Neighboring hexagons are rotated by around 60 degrees. Thus we obtain only heteroatomic interactions throughout the structure. The Rh–Ge distances within the polyanionic network range from 251 to 261 pm in LT-CeRhGe and from 259 to 269 pm in HT-CeRhGe, slightly longer than the sum of the covalent radii of 247 for Rh + Ge [22]. The cerium atoms bind to the rhodium atoms. Calculations of the crystal orbital Hamilton populations showed slightly stronger Ce–Rh bonding for the high-temperature phase [77].

The arrangement of the Rh_3Ge_3 hexagons for the two modifications of CeRhGe nicely underlines the broad flexibility of the TiNiSi-type structure. Besides the variation in the lattice parameters (they play a major role) also the positional parameters of the 4*c* (*x* 1/4 *z*) sites allow shifts of the atoms. This way, a given Ce*TX* phase obtains its optimal adjustment of the [*TX*] polyanionic network around the cerium atoms. Although in Table 1 a broad variety of Ce*TX* phases is listed, their range of existence with respect to the valence electron count (VEC) is limited. The lowest VEC of 15 occurs for CeRuSi and the highest one of 18 for HP-CeAuGe. Already the ZrNiAl-type Ce*TX* phases [14] showed such a small VEC range.

An important parameter concerns the coloring of the *T* and *X* atoms within the [*TX*] polyanionic network. This coloring is a consequence of the electronegativity difference and the charge distribution of *T* and *X*. The atom with the higher electronegativity or the one with the higher accumulation of electron density always takes the position with the maximum distance within the T_2X_2 rhombs which form through the puckering between adjacent hexagons (Fig. 2). Two examples with a switch in the tilt of the T_2X_2 rhomb are LT-CeRhGe (maximum distance for the germanium atoms) [77] and CeAuZn (maximum distance for the gold atoms) [65]. Consequently, we can call LT-CeRhGe a germanide, while CeAuZn can be considered an auride with partially negatively charged gold atoms. Nevertheless, in order to be comparable with the other Ce*TX* phases we keep the sum formula CeAuZn instead of CeZnAu (which better emphasizes the auride character) throughout this paper. These electronic peculiarities of the TiNiSi-type phases were studied for many representatives by Nuspl et al. on the basis of extended

Table 2: Ce–Ce and Ce–*T* distances for the Ce*TX* phases where the structures were refined from single crystal or powder diffraction data.

Compound	Ce–Ce/pm	Ce–*T*/pm	Reference
CeMgSn	405, 406	330–339	[50]
β-CePdZn	365, 385	295–314	[52]
CePtZn	366, 382	297–309	[20]
CeAuZn	365, 409	311–327	[65]
CePtAl	364, 378	294–323	[59]
HT-CeNiGa	336, 385	293–303	[63]
CeRhGa	359, 369	281–306	[67]
CeIrGa	358, 372	289–305	[67]
CeNiGe	367, 371	299–321	[74]
CeRhGe	335, 387	302–310	[76]
HT-CeRhGe	365, 372	304–317	[77]
CeIrGe	362, 373	295–317	[76]
HP-CeAuGe	368, 371	306–323	[45]
CeNiSn	379, 385	307–333	[37]
CePdSn	385, 399	315–324	[38]
CePtSn	383, 391	310–323	[39]
CeRhAs	378, 399	305–309	[17]
CeRhSb	379, 390	310–318	[89]
CeIrSb	377, 384	304–331	[32]

Hückel calculations [97, 98]. The Ce*TX* phases fit in seamlessly in this large family of compounds. For further crystal chemical details on TiNiSi phases we refer to other review articles [99–101].

Chemical bonding in the Ce*TX* phases is mainly dominated by the strongly covalent *T*–*X* interactions. This has been underlined in several studies [52, 54, 77, 102–104]. Important parameters that govern the magnetic ground state of the Ce*TX* phases are the Ce–Ce and Ce–*T* (Table 2) distances. For those phases where single crystal diffraction data is available we list these distances. The Ce–Ce distances cover the broad range from 335 to 409 pm. For comparison, the Ce–Ce distance in *fcc* cerium [105] is 365 pm. Except for the high-temperature modification of CeRhGe (335 pm Ce–Ce) [77], all Ce–Ce distances in the Ce*TX* phases are longer than the Hill limit of 340 pm for *f* electron localization [106]. The magnetic data will be discussed on this basis in the following chapter. The Ce–*T* distances show a smaller range from 281 to 339 pm. These distances depend on the size of the transition metal and the cerium valence. In the case of intermediate valent cerium (tendency towards smaller Ce^{4+}) one observes shorter Ce–*T* distances. In most cases (for electrostatic reasons) the more electronegative transition metal is the nearest neighbor for the cerium atom. Besides the Ce–Ce distance, also the Ce(4f)-*T*(*n*d) hybridization is one of the key parameters governing the magnetic and transport properties of the Ce*TX* phases.

Not all Ce*TX* phases show structural stability over the studied temperature and pressure ranges. HP-CeAuGe is formed from the NdPtSb-type normal-pressure modification [44] at pressures larger than 8.7 GPa [45]. This structural phase transition is accompanied by a discontinuous volume change of –2.5%. In contrast we observe decomposition of the TiNiSi-type phase under high-pressure conditions for the stannides Ce*T*Sn (*T* = Ni, Pd, Pt) [37–39]. Here, the high-pressure phases crystallize with the hexagonal ZrNiAl type. A temperature driven structural phase transition also occurs for CeNiGa [63] and CePdZn [52]. The ZrNiAl-type low-temperature modifications transform via reconstructive phase transitions to the TiNiSi-type high-temperature modifications and the latter can be quenched. The situation for CeRhGe [77] is more complex. One keeps the space group symmetry, and the first-order structural phase transition proceeds via drastic changes in the unit cell parameters as well as shifts in the atomic parameters.

The arsenide CeRhAs [17, 35, 36, 107, 108] shows three anomalies (T_1 = 370, T_2 = 235 and T_3 = 165 K) in the temperature dependence of the lattice parameters and also in the magnetic susceptibility data. Closer inspection of the unit cell parameters revealed that this anomaly mainly concerns the *a* lattice parameter, the pseudo-hexagonal axis along which the Rh_3As_3 hexagons are stacked. From room temperature on the *a* lattice parameter decreases from ca. 749 to ca. 739 pm [35], implying good compressibility of the CeRhAs structure along the *a* axis. For better understanding of this structural peculiarity we draw back to the interlayer rhombs discussed for CeRhGe (*vide ultra*). In Fig. 3 we present these rhombs for LT-CeRhGe, CeRhSb, CeRhGa, and CeRhAs (data from the room temperature structure refinement [17]). The different tilts of the rhombs of LT-CeRhGe, CeRhSb, and CeRhGa reflect the different

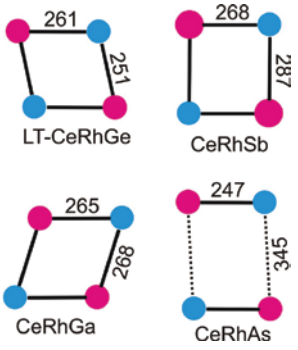

Fig. 3: Comparison of the interatomic distances (pm) in the Rh_2X_2 (*X* = Ge, Sb, Ga, As) rhombs in the structures of LT-CeRhGe, CeRhSb, CeRhGa, and CeRhAs. The transition metal and *X* atoms are drawn as blue and magenta circles, respectively.

electronic situation induced by the germanium, antimony and gallium atoms. The drastic difference for CeRhAs, however, concerns the huge inter-layer Rh–As distance of 345 pm, much longer than the sum of the covalent radii of 246 pm for Rh + As [22]. Thus we observe no inter-layer Rh–As bonding at room temperature and this readily explains the good compressibility along the *a* axis, leading to stronger puckering of the Rh_3As_3 hexagons and shortening of the inter-layer Rh–As bond. The consequences for the physical properties of CeRhAs are discussed in the following chapters.

Finally we turn back to two Ce*TX* phases that had initially been ascribed to the KHg_2 type with disorder, CePdGe and CePtGe [30, 69, 75, 78]. Careful reinvestigations on the basis of single crystal X-ray data revealed complete Pd/Ge and Pt/Ge ordering, however, slightly differing from the TiNiSi type. CePdGe [31] was ascribed to the CaCuGe type [24] and CePtGe [110] to the YPdSi structure [111]. While in all other Ce*TX* phases one observes exclusively *T*–*X* bonding between the hexagons, the ordering variants of CePdGe and CePtGe show weak Pd–Pd, Pt–Pt, and Ge–Ge inter-layer bonding. The sequence of the near-neighbors coordinations of the crystallographically different cerium atoms in both germanides are presented in Fig. 4.

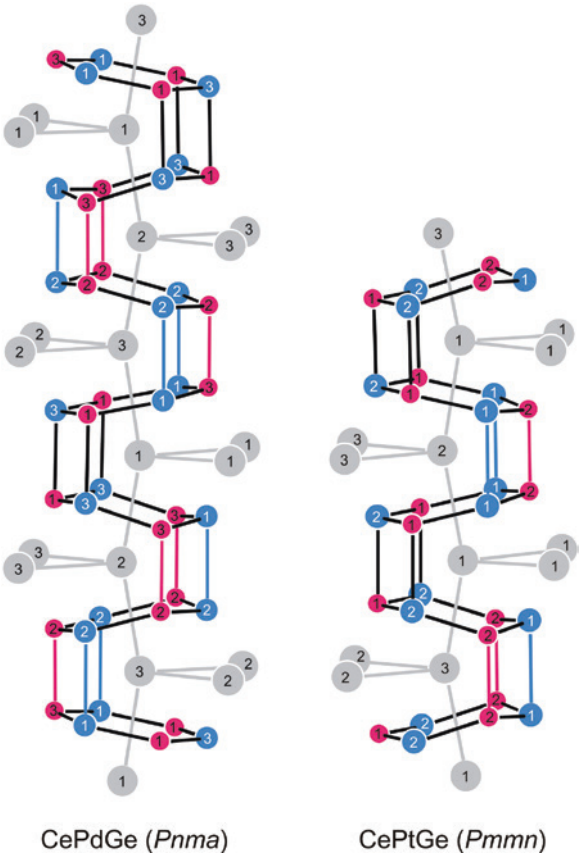

Fig. 4: Coordination of the cerium atoms in the structures of CePdGe [31] and CePtGe [110]. Cerium, rhodium, and germanium atoms are drawn as medium gray, blue, and magenta circles, respectively. The crystallographically independent sites are emphasized.

3.2 Physical properties

The main structural and electronic parameters that influence the magnetic ground states of the Ce*TX* intermetallics have been summarized and discussed in our previous review on the ZrNiAl-type Ce*TX* phases [14]. These reflections were based on the Doniach diagram [2, 118–120] and the Ce*TX* phases were roughly regrouped into three classes, i.e. (i) a normal localized Ce(4f) state along with a magnetic moment (called a magnetic RKKY metal) occurs if the Ce(4f) level lies below the Fermi level, (ii) a magnetic Kondo system, when the Ce(4f) level approaches the Fermi level, leading to a reduction of the magnetic ordering temperature and the magnetic moment, and (iii) a non-magnetic Kondo system in the case of a further increase of J_{cf} (hybridization between 4f and conduction electrons), leading to valence fluctuations.

In the following discussion we first review the magnetic and transport properties as well as the spectroscopic behavior of the pure Ce*TX* phases and then switch to their hydrogenation behavior and a summary of solid solutions with respect to the cerium, *T*, and *X* positions. We want to mention that we grouped the compounds in two large classes: (i) compounds exhibiting conventional magnetism and (ii) intermediate valence, valence fluctuations, Kondo compounds and heavy fermion materials. Within these groups we will give an overview of the measurements conducted for the individual compounds.

3.2.1 Ferromagnetic Ce*TX* compounds

We start with a summary of the group of materials which shows conventional long-range magnetic ordering. Amongst the large number of Ce*TX* compounds discussed in this review article only three compounds exhibit ferromagnetic ordering. These are CePtAl, CeAgAl and CeAgGa with Curie temperatures of ~6, ~3 and ~5 K, respectively. In the case of CePtAl a complex magnetic system was investigated by neutron powder diffraction and two coexisting, partly ferromagnetic and incommensurate magnetic structures and three magnetic phase transitions at T_1 = 5.9, T_2 = 4.3 and T_3 = 2.2 K have been

found [121]. While the transition at T_1 is of the second order, T_2 and T_3 are both first order phase transitions. For $T_2 < T < T_1$ the two magnetic propagation vectors were determined to be $k_1 = 0$ and $k_3 = [0, 0.463(8), 0]$, for $T < T_2$ the vectors $k_1 = 0$ and $k_2 = [0, 1/2, 0]$ were found. The complexity of the magnetic structure was ascribed to exchange interactions between two chains of Ce atoms with d(Ce–Ce) = 356 pm along the b axis and d(Ce–Ce) = 377 pm along the a axis. The effective magnetic moment was determined to be $\mu_{eff} = 2.58\ \mu_B$ per Ce atom and the Weiss constant of $\theta_p = 6.5$ K. Simulating the magnetic data revealed a Kramers doublet ground state [122]. In a subsequent paper single crystals of CePtAl grown by the Czochralsky method were investigated by high-field magnetization experiments up to 300 kOe (1 kOe = 7.96×10^4 A m^{-1}). Pronounced magnetic anisotropy was detected, which was attributed to crystalline–electric field interactions. The a axis corresponds to the easy axis while the hard axis changes from c ($T > 39$ K) to b ($T < 39$ K) [33]. Ueda et al. studied the de Haas-van Alphen effect in a high-quality single crystal of CePtAl by detection of the field modulation in fields up to 170 kOe and temperatures down to 30 mK. Their results suggest that the Fermi surfaces in CePtAl consist of multiply connected Fermi surfaces [34]. Finally the pressure dependence of the magnetic susceptibility was studied to determine the critical pressure p_c at which the magnetic ordering temperature becomes zero. In electrical resistivity measurements under pressure they observed a shift of the Kondo features which collapse > 6 GPa. The first ordering temperature follows this trend. It shifts to higher temperatures and disappears above 6 GPa [123–125].

As already discussed in the crystal chemistry part no crystallographic ordering is present in the silver compounds CeAgAl [54] and CeAgGa [126] for Ag and the main group element, thus influencing the physical properties. Both compounds show Curie–Weiss behavior and negative paramagnetic Curie temperatures of –18 [54] and –43 K [70], respectively. The large negative values are not due to antiferromagnetic interactions in the paramagnetic range, but a result of a crystalline electric field (CEF). The presence of a CEF effect has been proven for CeAgGa by inelastic neutron scattering [126]. However, the negative Weiss constants have also been attributed to Kondo interactions [54, 70] (*vide infra*). Referring to dc-susceptibility measurements magnetic ordering at T = 2.9 for CeAgAl [54], 5.5 [126], and 5.1 K [70] for CeAgGa have been reported. In accordance with the magnetization isotherms the magnetic ordering has ferromagnetic character. However, systematic ac-susceptibility measurements of CeAgGa showed maxima around 5 K with amplitudes and positions depending on the frequency of the applied magnetic field. The dependence of the maximum follows the Vogel–Fulcher law which is characteristic for a spin glass behavior. By measuring the isothermal remanent magnetization M_{IRM} as a function of time a canonical spin glass could be identified [70]. Further hints to a spin glass-like characteristic were found in the zero-field cooling (ZFC) and field cooling (FC) measurements as well as in the heat capacity. The ZFC/FC curves bifurcate already above T_f and the anomaly in specific heat capacity is a broad peak instead of a λ-anomaly. Furthermore, the shape of the anomaly is rounded and shifted to higher temperatures by applying magnetic fields [70]. Referring to the literature of spin glasses [127, 128] some important spin glass characteristics are fulfilled, however, a broad peak in the specific heat pattern is expected to be approximately 20% above T_f, which is not the case for CeAgGa.

An almost identical behavior can be observed for CeAgAl [54]. Though no ac-susceptiblity investigations were performed and some of the described features have been partially accounted for a Kondo behavior, a somehow spin glass-like behavior can also be predicted for CeAgAl due to the mixing of Ag and Al atoms on the 8*h* site. CeAgAl [54] and CeAgGa [70] have both been characterized as Kondo lattices. As reasons for this behavior the large negative value of the Weiss constants, the development of the magnetic entropy and the characteristic shape of the anomaly in the specific heat have been stated. In our opinion it should be considered that in cerium based Kondo lattices that exhibit a magnetic ordering, in general the specific heat is dominated by the magnetic ordering in contrast to the Kondo interactions. This, for instance, is the case for CePdSn (*vide infra*). Consequently, the development of the specific heat with increasing magnetic contribution is most likely caused by the spin glass character which was already considered for CeAgAl [54]. The large negative values of the Weiss constants can also be caused by CEF which has been nicely proven by inelastic neutron scattering [126]. Referring to the original publication by Kondo, a Kondo lattice is present if the resistivity shows a minimum and a logarithmic increase with decreasing temperature due to an additional scattering mechanism [129]. In cerium based Kondo lattices this minimum is often followed by a rapid decrease due to the magnetic ordering at lower temperatures. Such a drop due to the magnetic ordering definitely occurs for both compounds, but only a very weak minimum can be observed for CeAgAl. As a consequence we would be more cautious to define these compounds as Kondo lattices.

3.2.2 Antiferromagnetic Ce*TX* compounds

CeMgSn was reported to possess an antiferromagnetic ground state with an ordering temperature T_N = 12 K [26]. Investigations by high resolution neutron powder diffraction confirmed the AFM ground state and a Néel temperature of T_N = 13 K. No evidence for the Kondo effect was found in the temperature dependent resistivity measurements. The analysis of the difference spectrum between T = 2 K and 20 K revealed multiple magnetic peaks not corresponding to the nuclear Bragg peak positions, confirming the antiferromagnetic coupling. The magnetic propagation vector at 2 K was determined and refined to τ = [0, 0.1886(4), 0.3384(8)]. The maximum magnetic moment of the modulated structure was refined to 2.24(2) μ_B per Ce atom consistent with a strong localization of the $4f^1$ electron [50]. Almost the same different magnetic propagation vector of [0, 0.187, 0.340] for CeMgSn was observed at T = 40 K, an indication of an incommensurate antiferromagnetic structure [130].

The orthorhombic high-temperature β-form of CePdZn was found to order antiferromagnetically at T_N = 3.2(1) K. The effective magnetic moment was determined to μ_{eff} = 2.42(1) μ_B per Ce atom which is close to the theoretical value for the free Ce^{3+} ion. However, a positive Weiss constant was found suggesting ferromagnetic interactions in the paramagnetic region [52].

For the heavier homologue CePtZn [20] no magnetic ordering was observed in susceptibility or heat capacity measurements down to 2 K. The inverse magnetic susceptibility can be described by the Curie–Weiss law resulting in an effective magnetic moment of μ_{eff} = 2.47(1) μ_B per Ce atom. This clearly indicates trivalent cerium. The Weiss constant was found to be negative with θ_p = –18.7 K. Subsequent work on this system by Dhar and co-workers [21] revealed antiferromagnetic ordering at T_N = 1.7 K and Kondo behavior visible in the low temperature electrical resistivity with the Kondo temperature (T_K ~ 2 K) comparable to the ordering temperature. Field dependent resistivity measurements showed a suppression of the AFM transition around 50–60 kOe. The same suppression has been found in pressure dependent resistivity measurements. The authors suggest the appearance of a quantum critical point (QCP) with $T_N \rightarrow 0$ K, the experimental conditions (H = 120 kOe, p = 2.66 GPa) however were not sufficient to experimentally show the superconducting state. However, the QCP is assumed to be at p_c ~ 1.2 GPa and H_c ~ 60 kOe as seen from the non-Fermi liquid behavior [21]. Doping of CePtZn by small amounts of Au leads to an increase of the Néel temperature (T_N = 2.1 K) while in the case of Ni doping a drop to T_N = 1.1 K could be observed [117].

CeAuZn exhibits trivalent cerium with an effective magnetic moment of μ_{eff} = 2.51(1) μ_B per Ce atom. No Kondo behavior was observed in the electrical resistivity measurements and no magnetic ordering down to 2.1 K was observed by Hermes et al. [65]. Dhar et al. did also not observe a magnetic transition in susceptibility measurements, however heat capacity measurements revealed antiferromagnetic ordering at T_N = 1.7 K [117]. A fit of the region below 1.2 K yielded the electronic specific heat coefficient γ = 0.022 J mol^{-1} K^{-2}. This coefficient is significantly smaller than γ of CePtZn (0.6 J mol^{-1} K^{-2}), which has been explained by the relatively weak electronic correlations in CeAuZn and the changes in the electronic band structure near the Fermi level.

The magnetic properties of CeAuAl were first reported by Hulliger in 1993 [61]. He observed antiferromagnetic ordering with T_N = 3 K, a Weiss constant of θ_p = –13 K and an effective magnetic moment of μ_{eff} = 2.46 μ_B per Ce atom. A strong deviation from the Curie-Weiss law along with a magnetic transition near 34 kOe in the magnetization isotherms were noted as remarks. Kondo lattice behavior in this compound was reported later by Menon and Malik [62]. They observed AFM ordering at T_N = 3.8 K and the typical Kondo features in the temperature dependent electrical resistivity with a minimum at T_K ~ 20 K [62]. Heat capacity measurements confirmed the AFM ordering temperature. By subtraction of the heat capacity of LaAuAl from the one of CeAuAl the 4f contribution could be approximated. In the temperature range from 8 to 15 K, well above T_N, a large electronic contribution to the heat capacity of γ = 100 mJ mol^{-1} K^{-2} can be observed. Since crystal field splitting was absent, as known from inelastic neutron studies, the origin of this feature has to be attributed to the Kondo effect [131]. Inelastic neutron scattering studies [132] proved the existence of two well defined crystal field excitations at 24.2 and 45.8 meV. Since the line width of the inelastic peaks is significantly larger than the instrumental resolution, the presence of strong spin-lattice couplings has been deduced, presumably due to the interactions between the 4f electron and the conduction electrons. The magnetization experiments revealed similar results with an ordering temperature of T_N = 3.8 K, a Weiss constant of θ_p = –35 K and an effective magnetic moment μ_{eff} = 2.5 μ_B per Ce atom. Magnetization experiments at 1.7 K indicated a metamagnetic transition which becomes less pronounced at higher temperatures and disappears at 4.5 K. However, no clear sign for metamagnetism was observed in the 1.7 K magnetoresistance measurements. Between 4.2 and 14 K single-ion Kondo behavior is observed. At low temperatures the cerium ions can be treated as J = 1/2 impurities due to the first

excited CF level at 24.2 meV. From the magnetoresistance data the Kondo temperature was determined to $T_K = 3.6$ K. Finally the thermoelectric power has been determined, which is small and positive above 150 K but changes its sign with decreasing temperature showing a pronounced minimum at 50 K and finally moving towards 0 $\mu V\ K^{-1}$ for $T \rightarrow 0$ K [132].

CePtGa was reported to order antiferromagnetically with $T_N = 3.5$ K [131]. The influence of static pressure on the electrical resistivity was investigated later and a temperature dependence typical for a concentrated Kondo compound with a Kondo minimum at $T_K = 24$ K was found [134]. In the electrical resistivity data a decrease of T_N was observed with increasing pressure, however above 0.8 GPa the ordering phenomena disappeared. Magnetoresistance measurements revealed a negative sign which is consistent with an incoherent Kondo system. The sign stays negative with increasing pressure, but an extrapolation of the data suggests a crossover at 3 GPa [134, 135]. Susceptibility investigations on polycrystalline powdered samples showed essentially trivalent cerium ($\mu_{eff} = 2.36\ \mu_B$ per Ce atom) with a low saturation magnetization of $\mu_{sat} = 0.12\ \mu_B$ at 5 K and 30 kOe. No magnetic ordering was found by the authors, but a large negative paramagnetic Curie temperature of $\theta_p = -68$ K was observed. Crystal field studies via inelastic neutron scattering experiments at 11 K and 60 meV incident energy displayed two well-defined crystal field transitions near 18 and 36 meV (208 and 417 K). The ground state was found to be a well-separated Kramers doublet [136].

Heat capacity measurements on a single crystal specimen grown by the Czochralski method showed a λ-type anomaly at 3.4 K, consistent with the magnetic ordering temperature from susceptibility measurements. The results of the pressure dependent resistivity measurements conducted at the single crystal specimen were in good agreement with the ones from polycrystalline samples, also showing a decreasing Néel temperature [137]. The magnetic properties and the directional electrical resistivity of CePtGa have finally also been determined on single crystals. By their measurements, Shirakawa and co-workers were the first to explain the magnetic anisotropy caused by the CEF [113]. They investigated the magnetic susceptibility along the three principle axes as a function of temperature and found the antiferromagnetic ordering at $T_N = 3.5$ K. However, different critical fields for the spin reorientations were found. Along the *c* axis $H_{Cr} =$ 35 kOe was observed, while along the *a* axis a much higher field was needed. Directional resistivity measurements revealed a resistivity along the *b* axis which is about three times larger compared to the ones along the *a* and *c* axes. Furthermore the CEF was calculated from the fits of the χ^{-1} data giving energy separations of 294 and 559 K which are quite similar to the data obtained from inelastic neutron scattering experiments.

Measurements of the thermoelectric power of CePtGa showed only a small Seebeck coefficient due to the metallic nature of the material, but an inverse tilda-shaped trend was observed with an inversion of the sign between 50 and 100 K and a minimum at 26.7 K, consistent with the Kondo temperature found from resistivity measurements [138].

A slightly elevated Néel temperature of $T_N = 4.2$ K has been found for gallium deficient single crystals of $CePtGa_{1-x}$ [139] along with a strong magnetic response of the susceptibility when measured perpendicular to the *b* axis. Only a small response was seen when measured parallel to *b*. Therefore the Ce moments are expected to be in the *ac* plane. The Ga deficiency finally was estimated to be ~0.6 when assuming an effective magnetic moment equal to the theoretical moment of trivalent cerium. From heat capacity measurements $\gamma = 76$ mJ $mol^{-1}\ K^{-2}$ was extracted. Pressure dependent resistivity measurements revealed a positive increase of the Néel temperature with increasing pressure, contradictory to the negative shift observed before in polycrystalline CePtGa and stoichiometric single crystalline CePtGa [139]. The authors already noted a structural problem for the gallium deficient sample. Straightforward indexing of the powder pattern was not possible.

Stoichiometric polycrystalline CePtGa was synthesized by Kotsanidis et al. [140]. They measured magnetic susceptibility data above 5 K yielding an experimental magnetic moment of 2.36 μ_B per Ce atom.

CeRhGe was reported to be an antiferromagnetic Kondo compound with an ordering temperature of $T_N = 9.3$ K [30]. Susceptibility measurements showed an anomaly while magnetization experiments below 11 K with fields up to 50 kOe clearly indicated antiferromagnetism. The reduced effective paramagnetic moment $\mu_{eff} = 2.30\ \mu_B$ and the large Weiss constant ($\theta_p = -56$ K) were extracted by applying the Curie–Weiss law to the high temperature data (>130 K). The low effective magnetic moment was attributed to crystal field splitting effects while the large negative Weiss constant is consistent with Kondo behavior. Additional heat capacity and electrical resistivity measurements confirmed the ordering phenomena with consistent temperatures of $T = 9.3$ and $T = 9.2$ K, respectively. The λ-shape indicates a second-order magnetic phase transition, while the low temperature specific heat (<3.5 K) shows an enhanced electronic contribution $\gamma =$ 75 mJ $mol^{-1}\ K^{-2}$ clearly suggesting Kondo behavior.

Heat capacity measurements on single crystals confirmed the λ-anomaly, the electronic contribution was determined to be $\gamma = 47$ mJ mol^{-1} K^{-2} [141]. The resistivity measurements, however, did not show a clear Kondo minimum but rather a double-peak structure with the maximum at 150 K attributed to the crystal electric field, and the shoulder between 15 and 30 K attributed to the onset of coherency of the Kondo lattice [30]. The transition temperature and effective magnetic moment were confirmed later along with the field for the spin reorientation at $H_{Cr} = 25$ kOe [142]. In neutron diffraction experiments at $T = 1.7$ K one additional magnetic reflection was observed which was indexed as (100). The only possible explanation of the presence of this magnetic reflection is that the magnetic moments are aligned along the *b* axis. The additional magnetic reflections caused by this model are rather weak and therefore hard to observe [143]. Pressure dependent resistivity studies revealed an increasing peak at T_N in the resistivity with increasing pressure, but above the critical pressure $p_c = 1.9$ GPa this feature disappears and the Néel temperature becomes zero [144]. A later work, in which single crystals were used, the resistivity peak was associated with the formation of a spin density wave. The magnetic structure, when determined from single crystals, furthermore was found to be incommensurate with k = [−0.0606, −0.1168, 0.9062]. Directional magnetization experiments suggest that the crystallographic *a* axis is the easy-axis which also shows two spin reorientations at 80 and 130 kOe. The other directions show a linear field dependency. The effective magnetic moment along *a* is close to the calculated one for trivalent cerium ($\mu_{eff} = 2.49\ \mu_B$), however it strongly deviates for H || *b* and *c*. The authors suggest strong CEF, roughly estimated to be 1000 K [145]. With the help of theory and the operator method, Li and co-workers calculated the energy levels caused by the CEF for CeRhGe by fitting the experimental data from Ueda et al. [145]. They found that the sixfold degenerated 4*f* levels of a Ce^{3+} ion are split into three Kramers' doublets and the total excited energy was calculated to be 970 K (the splitting of these state is usually given on the K scale) which is in good agreement of the values reported earlier [146].

CePdGe was reported to be an antiferromagnetic material with $T_N = 3.4$ K, determined by susceptibility and heat capacity measurements [30]. The effective moment was determined to be $\mu_{eff} = 2.55\ \mu_B$ and the Weiss constant of $\theta_p = -37$ K was extracted by applying the Curie–Weiss law to the data >60 K. Resistivity measurements also show an anomaly at $T = 3.4$ K, consistent with the magnetic data. Neutron diffraction data collected at 2 and 5 K showed two reflections of low intensity indexed by a vector k = (0.42, 0, 0). This vector corresponds to a linear spin wave where the moments are aligned along the *b* axis [147]. Similar magnetic results were presented by Kotsanidis et al. [148]. At this point it is worthwhile to note that the magnetic structure studies were based on the wrong subcell structure. As emphasized in the crystal chemical part, tripling of the subcell structure is observed for the ordered nuclear structure of CePdGe and thus, the translation in the magnetic structure cannot be shorter than in the nuclear one.

CePtGe orders antiferromagnetically at $T_N = 3.4$ K with trivalent cerium ($\mu_{eff} = 2.54\ \mu_B$) derived from Curie-Weiss fits above 90 K. The large negative Weiss constant $\theta_p = -82$ K was ascribed to the presence of the Kondo effect, however the electrical resistivity shows no Kondo minimum but a double peak structure with a peak at $T = 3.4$ K, consistent with the susceptibility data. As for CePdGe the magnetic ordering was observed without doubt in the heat capacity measurements showing a λ-shaped anomaly [30]. Further studies regarding the pressure dependence of CePtGe revealed a lowering of the shoulder with increasing pressure, $dp(T)/T$ is zero at $p_C = 17.4$ kbar. The magnetic transition temperature changes only little from $T_N = 3.36$ K at ambient pressure to $T_N = 3.77$ K at $p = 13.1$ kbar [149]. Investigations regarding the ratio of T_K to T_N showed that CePdGe and CePtGe fit the trend observed for other Kondo compounds like, e.g. $CePd_2Ge_2$, $CePd_2Si_2$ or $CePd_2Sn_2$ [150]. The Seebeck coefficient shows an inversion of the sign with a positive peak at ~100 K and a minimum at 10 K followed by a rise to 0 μV K^{-1} for $T \rightarrow 0$ K [149], similar to [133].

CePdSn exhibits an antiferromagnetic phase transition at $T_N = 7.5$ K, much higher than expected, especially when compared to the isostructural Gd compound (T_N = 14.5 K) suggesting strong hybridization between the Ce 4f and the conduction electrons. From the susceptibility data above 50 K the effective magnetic moment was determined to be close to that of free Ce^{3+} ions while the Weiss constant $\theta_p = -68$ K is significantly larger than the Néel temperature. Magnetization experiments revealed a linear field dependency with no hint for saturation up to 8 kOe. Heat capacity measurements confirmed the magnetic data and a λ-shape anomaly was found with a maximum ~7 K. The entropy of this transition was estimated from C/T vs. T plots to be ~4.3 J mol^{-1} K^{-1}. Finally electrical resistivity measurements were conducted proving the Kondo effect in CePdSn due to a minimum in the resistivity data at $T_K = 20$ K [151, 84]. The magnetic ordering has been confirmed by Kyogaku et al. by ^{119}Sn NMR experiments [152]. The magnetic entropy of CePdSn was obtained by subtracting the value for LaPdSn from the total entropy of

CePdSn. Above the ordering temperature R ln 2 behavior is found confirming the postulated doublet ground state. The electronic specific heat coefficient was determined to $\gamma = 60$ mJ mol^{-1} K^{-2}, again proving the presence of a dense Kondo effect. Furthermore neutron diffraction experiments were conducted suggesting that the magnetic structure is a simple spiral one with a propagation vector of k = [0, 0.473, 0] [153]. High pressure experiments revealed that above 6 GPa the sharp ordering feature visible in the electrical resistivity disappears [154]. Here we should keep in mind that the structural phase transition to HP-CePdSn proceeds at 10.5 GPa [38].

CePtSn orders antiferromagnetically with two transitions at 7.8 and 5.5 K, respectively. The effective magnetic moment $\mu_{eff} = 2.85\ \mu_B$ is higher than expected, the Weiss constant $\theta_p = -9.2$ K is in good agreement with the ordering temperature. The magnetization can be described as a linear function of the magnetic field strength at 4.2 K [155]. Neutron diffraction experiments conducted at 1.7 K showed additional reflections in agreement with the antiferromagnetism [156]. Analysis of the data suggests that the moment is parallel to the b axis, as (0 k 0) reflections were found to be systematically absent. Inelastic neutron scattering showed two well defined crystal field excitations at 24.0 and 34.9 meV (278 and 404 K). Resistivity measurements indicated a Kondo minimum at T_K = 20 K followed by a sharp drop at the ordering temperature. The magnetic scattering part of the resistivity was determined by subtracting the resistivity of LaPtSn from the one of CePtSn and shows two different temperature regimes in the ln(T) plots. This was attributed to the Kondo effect arising from the CEF splitting of the ground state [156]. The propagation vector was later determined to be k = [0, 0.428, 0] at 1.7 K with a linear transverse spin wave character and the moments aligned along the c axis which is in contrast to the observations reported before [152]. Single crystal neutron studies of CePtSn showed a magnetic phase transition at T = 3.8 K with an incommensurate wave vector k = [0, 0.466, 0], above the magnetic order at k = [0, 0.418, 0] [157]. ^{119}Sn NMR investigations found the NMR signal to suddenly disappear below T_N. A correlation between the Knight shift of the ^{119}Sn and ^{195}Pt signals revealed a strong temperature dependence of both signals. However, the shift dependency at higher temperatures is linear. The hyperfine coupling constants were estimated to 9.8 kOe μ_B^{-1} for ^{119}Sn and 10.5 kOe μ_B^{-1} for ^{195}Pt. These values tell, compared to 26 kOe μ_B^{-1} for CeNiSn, that the s-f hybridization is weaker compared to CeNiSn. The 4f electrons are not so significantly affected by the hybridization, exhibiting more localized character [152].

Sakurai et al. were the first to report that CePdGa shows an antiferromagnetic transition around 2.2 K [133]. The trivalent state of cerium was determined by inelastic neutron scattering experiments. Two well defined transitions can be found at 18.9 and 33.8 meV indicating a well-localized f electron in CePdGa [158]. Susceptibility measurements showed Curie-Weiss behavior in the temperature range of 180–300 K. Below 180 K a strong deviation can be found which was attributed to crystal electric field splitting. Furthermore the magnetic contribution to the electrical resistivity was determined by subtracting the resistivity of LaPdGa from the data obtained from CePdGa. A ln T dependence was found for the high as well as for the low temperature regime. This observation was explained by a Kondo effect in the presence of crystal electric field [159, 160]. Measurements of the Seebeck coefficient revealed a broad maximum at 170 K followed by a sign change at 77 K and a minimum at 23 K [158]. Low temperature investigations down to 70 mK of the specific heat of CePdGa confirmed the antiferromagnetic transition at a slightly lower Neél temperature T_N = 1.8 K. The specific heat data <200 mK was used to determine the electronic contribution of the specific heat to be $\gamma = 372$ mJ mol^{-1} K^{-2}. The large value was attributed to heavy fermion behavior. The heat capacity data also shows a small hump at ~1 K. This feature was attributed to the thermal population of spin waves in the antiferromagnetic state. The low temperature specific heat data was interpreted to be either a re-ordering of the localized 4f electrons or a competition of the formation of a heavy fermion state and the antiferromagnetic ordering. Thermal conductivity measurements showed a well-defined temperature dependence even at low temperatures. While at lowest temperatures κ is dominated by electronic transport the magnetic contribution becomes more and more dominant above $T > 1$ K exhibiting a nearly logarithmic behavior [161]. This logarithmic trend is seen for temperatures that are low when compared to the overall crystal field splitting parameter Δ [162].

3.2.3 Ce*TX* compounds with intermediate valence

Now we want to focus on the second group of compounds – intermediate valence, valence-fluctuating compounds, Kondo compounds and heavy fermion materials. Initially for CeIrAl the cerium atom was reported to be close to tetravalent [55]. Later investigations however revealed mixed-valent behavior with a very high Kondo temperature of T_K ~1300 K obtained by comparing the susceptibility with other results from the literature. At the Kondo

temperature hybridization effects between the 4f electrons and the conduction electrons start to take place leading to the formation of a singlet ground state at low temperatures and therefore a quenching of the magnetic moments of the 4f electrons. Consequently no magnetic ordering down to 2 K was detected. The measured resistivity shows, in contrast to CeRhSb, no rise at low temperatures. Instead the typical behavior of a metal is found without a pronounced Kondo minimum between 2 and 300 K [57].

CeRhGa was first reported by Hulliger to be non-magnetic with a cerium valence state being close to tetravalent [68]. More detailed studies showed that the magnetic susceptibility above 75 K is nearly temperature independent. This characterizes CeRhGa as an intermediate valent system with a high Kondo temperature. From the susceptibility measurements a Kondo temperature was estimated to be T_K = 420 K [67]. Goraus et al. [66] investigated CeRhGa by various methods and determined the Weiss constant θ_p ~ 8 K and the effective magnetic moment μ_{eff} = 1.5 μ_B, which is significantly lower than that of trivalent cerium. With the help of the Sales and Wohlleben model [163] the intrinsic part of the susceptibility and the interconfiguration fluctuation temperature T_{sf} ~ 500 K were determined. The low temperature part of the heat capacity measurements in zero-field could be fitted and the electronic contribution to the heat capacity of γ = 38.3 mJ mol^{-1} K^{-2} was obtained. The small value of γ is typical for non-magnetic mixed valent compounds. For the full temperature range $C(T)$ could be fitted by the Debye expression. From the reasonable value of the Debye temperature θ_D ~ 239 K and the number of atoms in the formula unit, the authors concluded that the CEF contribution to the specific heat is small. Resistivity measurements did not indicate a typical Kondo behavior. The low temperature part gave rise to the assumption of Fermi liquid behavior. XPS measurements revealed the presence of $3d^9_{5/2}$ $4f^1$ and $3d^9_{3/2}$ $4f^1$ states for the Ce^{3+} ions, and additionally $3d^9$ $4f^2$ and $3d^9$ $4f^0$ states were visible. This underlines the interatomic hybridization between the 4f states and the conduction band. The occupation of the 4f state was finally calculated to be n_f ~ 0.9 [66].

Both modifications of CeNiGa [63] have been characterized as intermediate valence systems. While LT-CeNiGa crystallizes in the hexagonal ZrNiAl-type structure, HT-CeNiGa was found to be orthorhombic with TiNiSi-type structure. Magnetic measurements of HT-CeNiGa above 100 K showed Curie–Weiss behavior. An effective magnetic moment of μ_{eff} = 2.70 μ_B and a large negative Weiss constant of θ_p = –162 K were found. Between 60 and 20 K a slow increase is visible while <20 K a sharp increase with decreasing temperature was observed. The low-temperature feature was attributed to impurities of Ce^{3+} which were determined and subtracted from the low-temperature data. The corrected data can be interpreted as local spin fluctuations as a result of either Kondo interactions or valence fluctuations. The Kondo temperature was furthermore estimated to be T_K = 95(5) K. In comparison, the significantly lower Kondo temperature of HT-CeNiGa compared to CeNiAl (T_K ~ 1000 K) can be interpreted as a less pronounced mixing of the Ce 4f and the conduction band states. The electrical resistivity data confirms the intermediate valence behavior because the low temperature data between 4.2 and 150 K shows a negative curvature while the data above 150 K is temperature independent [63].

CeNiGe was found to exhibit a paramagnetic ground state since no magnetic ordering phenomenon was observed down to 4.2 K. Susceptibility measurements revealed significant contributions of Ce^{3+} impurities masking the actual ground state. High field measurements at 350 kOe were used to estimate the temperature dependence of the intrinsic susceptibility. A rather flat maximum was found indicating an intermediate valence state for cerium. Heat capacity measurements showed an electronic contribution of γ = 32 mJ mol^{-1} K^{-2} which gives direct evidence to the presence of 4f states at the Fermi level [164]. Seebeck investigations showed that the region below room temperature may be one side of a single and positive peak with a large width. For $T \rightarrow 0$ the Seebeck coefficient also approaches zero, as seen for other intermediate valence compounds. The maximum of S could be correlated with the Kondo temperature T_K, while for $T < T_K$ a non-magnetic Kondo state is realized [165].

Susceptibility measurements of CeIrGe revealed non Curie–Weiss behavior and a strong variation of the inverse susceptibility, which was fitted and μ_{eff} = 0.27 μ_B and a Weiss constant of θ_p = –10 K extracted. The small effective moment can be interpreted as delocalized 4f electrons and therefore a nearly tetravalent cerium ion. This is furthermore in good agreement with the determined lattice parameters of CeIrGe. The resistivity shows a quadratic temperature dependence below 50 K and a negative curvature at high temperatures, similar to other reported compounds [30, 166].

Sasakawa et al. were the first to report the physical properties of CeIrSb in 2005 [167]. They investigated the material with the help of susceptibility, heat capacity, resistivity and Seebeck measurements. However, their samples were contaminated with traces of CeSb which was visible in some of their measurements. From the magnetic measurements no magnetic ordering was visible and a strongly curved shape of the inverse susceptibility

suggesting valence fluctuations. The large Weiss constant of $\theta_p = -1300$ K determined above 250 K is in line with the valence fluctuation. Resistivity measurements showed a curved gradual decrease of $\rho(T)$ typical for valence fluctuation compounds along with an anomaly at 20 K which was attributed to the impurity phase CeSb. The increase of the resistivity below 8 K was, in contrast to CeRhSb, not attributed to a gap formation but to carrier localization effects. The reason for this assumption is that the Seebeck coefficient S would show a large peak. Instead S(T) is positive down to 4 K and has a value of 40 μV K^{-1} for a wide temperature range (100–300 K).

Heat capacity measurements below 6 K show an electronic contribution with $\gamma = 10$ mJ mol^{-1} K^{-2}, suggesting strongly localized 4f states [167]. Later Kawasaki and co-workers investigated CeIrSb with the help of Sb NMR and NQR experiments and found the formation of a pseudogap at the Fermi level. At 4.2 K two transitions are observed for ^{121}Sb ($I = 5/2$) and three for ^{123}Sb ($I = 7/2$), respectively. The temperature dependence of $1/T_1T$ for CeIrSb has a maximum at 300 K and decreases significantly below this temperature. Below 4 K a short upturn is observed. The decrease of $1/T_1T$ was attributed to the energy gap at low temperatures. The upturn in $1/T_1T$ was assigned to the relaxation process of spin fluctuations of the paramagnetic Ce spins. The spin flipping – and hence the upturn – was suppressed by applying a small external magnetic field of 1 kOe. Due to the similarities in the temperature dependences of CeIrSb and CeRhSb the V-shaped gap model was used to determine the bandwidth D = 1800 K and the energy gap Δ = 350 K. Both, D and Δ, are significantly larger (up to one order of magnitude) compared to the values determined for CeRhSb and CeNiSn. The much larger value of D was assigned to the weaker temperature dependence of the magnetic susceptibility and a stronger crystal field hybridization as well as a much larger magnitude of the energy gap. Finally ^{121}Sb NMR investigations in high magnetic field and at $T = 10$ K were conducted. Six peaks are found in the field-swept measurement of the polycrystalline sample, which all show neither peak broadening nor splitting down to 5 K indicating a non-magnetic ground state for CeIrSb. The relaxation rates of the central resonance lines are furthermore field-independent up to 100 kOe indicating that the gap structure is not affected by the applied magnetic field [168, 169].

In addition to the structural investigations on equiatomic CeCuZn, the solid solution $Ce(Cu_{1-x}Zn_x)_2$ with $x = 0$–1 was investigated with respect to the physical properties. However, for the equiatomic CeCuZn no detailed study was conducted [170].

Similar to CeCuZn the solid solution $Ce(Cu_xGa_{1-x})_2$ was investigated regarding its physical properties. Besides binary $CeCu_2$, samples with $x = 0.95$, 0.9–0.5 were prepared and measured. The shallow minimum in the electrical resistivity found for $CeCu_2$ increases with increasing Ga content $x = 0.95$–0.6. For $x = 0.5$ the magnetic contribution was plotted versus the electrical resistivity in a semi logarithmic way. Two different temperature ranges are clearly visible showing −ln T behavior, reflecting Kondo-type interactions in the presence of strong crystal field splitting effects according to Cornut and Coqblin [159].

For CeCuGa a quartet ground state has been found while $CeCu_2$ exhibits a doublet ground state [171]. No magnetic ordering has been found for any member of the $Ce(Cu_xGa_{1-x})_2$ series with $x = 0.95$–0.5 caused by the evolution of the Kondo effect. The absence of magnetic ordering was also confirmed by heat capacity measurements. For CeCuGa a large electronic contribution to the heat capacity of $\gamma = 110$ mJ mol^{-1} K^{-2} has been extracted [172]. The magnetic moment of CeCuGa was determined to be $\mu_{eff} = 2.14\ \mu_B$ and therefore below the theoretical value of $\mu_{eff} = 2.54\ \mu_B$ for a trivalent cerium ion. However no indication for dynamical mixed valence or valence fluctutations was found. Also no superconductivity was found down to 0.5 K. The ratio of C/T increases remarkably below 10 K with a peak typical for Kondo compounds. This peak indicates a contribution of the localized magnetic moments to the specific heat [173, 174].

Nanocrystalline powders of CeCuGa with an average particle size of 9 nm were prepared by mixalloy processing. From their magnetic susceptibility above 18.5 K an effective magnetic moment of $\mu_{eff} = 2.45\ \mu_B$ per Ce ion and a Weiss constant of $\theta_p = -63$ K were extracted. From the square of the magnetization versus temperature a Curie temperature of 18.5 K was determined indicating weak antiferromagnetic ordering (considering the negative Weiss constant) below 18.5 K. From magnetization experiments with two external fields the authors concluded that the Kondo effect is not completely suppressed at $H =$ 500 Oe by the disorder within the nanocrystalline material since the M–T curves show two extremes at 3 and 15 K. However, already at $H = 5$ kOe, this change disappears [175]. Resistivity investigations at very low temperatures (0.5–150 K) showed a minimum at 25 K followed by a slight increase with decreasing temperature. At 3 K the resistivity passes a maximum which is expected if the coherent scattering of the conduction electrons by the magnetic moments leads to a decrease in resistance. The final decrease suggests that the ground state is associated with a Fermi liquid state. The specific heat measurements were carried out down to 80 mK with a hump at 1 K. Below

1 K it decreases before it increases again below 250 mK due to the significant contribution of the nuclear part of the specific heat. The electronic coefficient of the specific heat is extremely high (γ = 1200 mJ mol^{-1} K^{-2}), in line with CeCuGa being a heavy fermion material. γ is reduced when the specific heat is determined in the presence of a magnetic field. The authors stress that this behavior is not caused by a spin glass state as mentioned in previous literature [176], because the peak of the specific heat should be shifting to higher temperature in the presence of applied magnetic fields [177].

Hulliger was the first to report that for CeIrGa the cerium valence is between three and four at room temperature [68]. CeIrGa has been studied furthermore by powder X-ray diffraction and the volume of the unit cell was found to be almost the same as the one reported for CeIrAl. Therefore a mixed-valence state of the cerium ions was assumed. Susceptibility measurements revealed very low values for the magnetic susceptibility ($\chi \sim 10^{-3}$ emu mol^{-1}) at low temperatures [71]. A clear increase of χ was found above $T > 120$ K, suggesting a maximum in the susceptibility well above room temperature. A very similar behavior was found for CeIrAl indicating that CeIrGa also exhibits Kondo interactions. With the help of Rajan's curve [178] the Kondo temperature was estimated to be $T_K \sim 1000$ K [71].

By a number of complementary measurements [179] CeRuSi has been characterized as a heavy fermion compound. Susceptibility measurements revealed an effective magnetic moment of μ_{eff} = 2.43 μ_B and a Weiss constant of θ_p = –91 K, with a Curie–Weiss-type behavior down to 20 K. At low temperatures the susceptibility flattens off reaching a broad maximum at T = 8 K (1 kOe). At 45 kOe the maximum becomes better defined. Resistivity measurements revealed a maximum at slightly higher temperatures compared to the maximum observed at T = 50 K in Seebeck measurements. Furthermore a minimum at 5 K was observed. The reported value of S is about 20% higher compared to literature data [180]. Specific heat measurements have shown a broad maximum centered around 5.5 K. The Sommerfeld coefficient was calculated to be $\gamma \sim 0.18$ mJ mol^{-1} K^2 confirming the heavy Fermion character of the compound.

Before we summarize the physical properties of CeNiSn, we need to point out that this stannide has attracted tremendous attention, mostly for its physical properties. More than 230 entries are listed in the Scifinder data base [181]. In the following we focus on the most important contributions keeping the publication dates in mind. The papers dealing with solid solutions are addressed separately in section 3.5.

The first reports on CeNiSn by Scolozdra et al. and Takabatake et al. characterized the compound as an intermediate valence material [182, 183]. The susceptibility deviates from the classical Curie–Weiss behavior below 120 K with a reported effective magnetic moment of μ_{eff} = 2.86 μ_B [182]. The Weiss constant was determined to be θ_p = –187 K, and the magnetization at 1.3 K and 100 kOe was estimated to be only μ = 0.115 μ_B [183]. Resistivity measurements below 30 K showed an increase by a factor of four with saturation near 0.7 K. A lnρ vs. 1/T plot between 3 and 65 K gave an activation energy of 6 K, corresponding to a small energy band gap of 0.5 meV near the Fermi level. The specific heat measurements did not show any pronounced peak down to 0.45 K, and a C/T vs. T plot revealed a broad peak near 1.3 K, consistent with a gap of 0.5 meV. The electronic contribution was determined to γ = 120 mJ mol^{-1} K^{-2}, suggesting the compound to be a heavy fermion material [183].

Substitution of Ce by La in the solid solution $Ce_xLa_{1-x}NiSn$ suppresses the gap formation. While for CeNiSn $\epsilon_g \sim 3$ K was determined from resistivity measurements, $Ce_{0.9}La_{0.1}NiSn$ has an energy gap of ϵ_g = 1.6 K. With γ = 200 mJ mol^{-1} K^{-2}, the heavy fermion character was confirmed [184]. Following these initial findings, a large number of papers have been published concerning the physical properties of CeNiSn. In this work, often solid solutions have been used to investigate and understand the unique properties of CeNiSn, the properties of the respective members of the solid solutions and the depression of the gap via chemical substitution (*vide infra*). However, also physical pressure can be used to suppress the gap formation, since the application of pressure increases the hybridization between the 4f orbitals and the conduction electrons. The electrical resistivity under hydrostatic pressure up to 24 kbar was measured on a polycrystalline sample of CeNiSn. The strong increase below 30 K at ambient pressure is suppressed and a maximum at around 100 K arises. No indication for magnetic ordering under pressure has been observed. In order to determine the variation of the energy gap with pressure, lnρ vs. 1/T was plotted, giving a decrease of –0.02 meV kbar^{-1}, but the linear dependence does not hold below 7 K. The energy gap therefore seems to vanish around 30 kbar [185]. The hybridization of the 4f orbitals and the conduction electrons gives rise to a peak near the Fermi energy E_F and can therefore be investigated by Seebeck measurements, which are sensitive to the energy dependence of the density of states. The investigations of S vs. T on a single crystal of CeNiSn have shown a large anisotropy along the three different crystallographic axes. While S shows very sharp peaks

along *a* and *c* at 3 K, a broad peak at 100 K along *b* was observed [186].

^{119}Sn NMR investigations in the temperature range of 0.38–250 K excluded unambiguously the possibility of a magnetic phase transition down to 0.38 K. Analysis of the NMR data indicated furthermore, that the energy gap of CeNiSn is formed at the Fermi level, and that the picture of a Fermi liquid is not applicable. From the hyperfine coupling constant (26 kOe per μ_B), Fermi contact interactions of the 5s electrons with the polarized Ce4f electrons were derived [187–189]. Inelastic neutron studies at 15 and 50 K showed two distinct excitations at 3.5 and 6 meV, whereas the 6 meV excited state was also confirmed by transport property measurements. Interestingly, the spectra recorded at 4.5 and 8.8 K are flat in the range of 2–9 meV indicating the absence of magnetic scattering. This feature was attributed to the partial delocalization of the 4f electrons below 10 K [190]. No well-defined crystal field excitations were observed in other measurements as well [191].

By contrast the inelastic response of CeNiSn was described as rather structureless showing quasi-elastic scattering with large linewidths [192]. Neutron scattering measurements showed that the crossover at $T < 10$ K from a metallic heavy fermion state to a semiconducting state coincides with the formation of a spin gap in the magnetic excitation spectrum [193]. Thermal expansion measurements revealed an intriguing feature below 2 K. The thermal expansion coefficient α goes through a maximum at $T = 1.3$ K and changes its sign below 1 K. The amplitude of the negative α(T) anomaly is unusually large but down to 0.5 K no minimum was found. Furthermore a strong phonon line at $w \sim 343$ cm^{-1} was found in energy dependent reflection measurements. The phonon line gets sharper with decreasing temperature, but no splitting was observed below the proposed temperature for magnetic correlations [194]. Pressure dependent thermal expansion coefficient studies on a single crystal were conducted up to 8 kbar in the temperature range 4.2–300 K. The thermal expansion coefficients are highly anisotropic, reflecting the orthorhombic crystal structure, with a sharp peak at 6.5 K for α_b and a shoulder at 8 K for α_a. The anomalies were interpreted to be a result of the opening of the anisotropic energy gap. However, at 8 kbar both anomalies disappear [195].

Theoretical investigations, carried out by self-consistent LAPW calculations, found CeNiSn to be a semimetal with a hole Fermi surface [196, 197]. The temperature dependence of the elastic constants of CeNiSn was studied without and with an applied magnetic field. Without field, the elastic longitudinal constants C_{11} and C_{22} which correspond to the crystallographic *a* and *b* axes show a pronounced softening around 200 K before becoming stiff at about 40 K again. In contrast, C_{33} exhibits a shallow minimum at 180 K, showing the anomalous behavior of this compound, and the transverse C_{44}, C_{55} and C_{66} modes show no elastic softening. In ultrasonic experiments, no sign of magnetic ordering was detected down to 0.4 K. The anomalous behavior of the longitudinal modes was related to the quasiparticle band at the Fermi level. The monotonic increase of the transverse modes confirms the delocalization of the 4f electrons. Magnetic field effects on the longitudinal C_{11} mode showed a remarkable effect with respect to the *a* axis while little dependencies were observed along *b* and *c*. By contrast, C_{22} and C_{33} show the same anisotropic behavior upon applied field [85].

The mechanism of the gap formation was also studied by Hall and magnetoresistance measurements on single crystals. For the Hall coefficient, all the directions show an increase below 100 K, followed by a sharp drop to negative values. Since the peak temperature of R_H in heavy fermion systems is regarded as the onset of coherence, it was followed that CeNiSn gradually enters a coherent scattering regime below 9 K. However, the strong decrease below 5 K can be ascribed to a diminishing carrier density. Assuming only one type of charge carriers, the concentration was estimated to be 4.6×10^{-3} charge carriers per formula unit for $H \parallel c$ at 1.3 K. For the magnetoresistance ρ_a, a maximum near 11.4 K was observed, which gets smeared out in a field of 140 kOe for $H \parallel a$. The upturn below 10 K gets strongly suppressed. A large effect can be found in ρ_b for $H \parallel a$ indicating a metallic behavior, which is in contrast to the semiconductor-like behavior for $H \parallel c$ [198–200].

Photoemission studies on CeNiSn showed two prominent structures in the Ce 4f derived spectra (on-resonance minus off-resonance) around 2.5 eV and near E_F, respectively. The fairly high intensity of the feature near the Fermi level is consistent with the otherwise observed mixed-valent behavior. However, the valence of cerium is very close to +3 with an occupation of the trivalent state >0.95. The valence band photoemission spectra show the Ni 3d emissions at 1.5 eV along with a shoulder near E_F. The shoulder is caused by the hybridization of empty Sn 5p and filled Ni 3d states. This model has been underlined by Ni 3p $\rightarrow$ 3d on-resonance, off-resonance and Ni $2p_{3/2}$ core level spectra. They exhibit two hole satellites, which occur when the Ni 3d band is not completely filled. Since the Ni 3d band does not substantially cross E_F, the hybridization with the Sn 5p band, which leads to depleting of the 3d states can be derived [201]. Additional investigations of the Ce 4d core level showed a main feature between 105

and 115 eV, originating from the final Ce $4d^9 4f^1$ states, along with a hump at 120 eV which can be assigned to the Ce $4d^9 4f^0$ states, underlining the mixed valent character. Ce 3d core level spectra showed two strong peaks at the binding energies of about 884 and 903 eV, which can be assigned to the $3d_{5/2}$-$3d_{3/2}$ spin-orbit components of the $3d^9 4f^1$ final states [202]. With the help of ^{119}Sn Mössbauer and μSR spectroscopy techniques the so-called transferred hyperfine field was determined. The muon senses the magnitude and the distribution of the magnetic field on an interstitial site. The ^{119}Sn Mössbauer spectra of CeNiSn show no magnetic interaction down to 1.5 K. The spectral shape arises solely from the quadrupole interaction due to the non-cubic local symmetry. For the zero-, longitudinal- and transverse-field μSR measurements of a single crystal of CeNiSn, no influence of the magnetic moments of Ce could be detected above 2 K. At $T < 1$ K, a continuous change in the muon relaxation is observed, which is typical for a paramagnet approaching the magnetic order. However down to 33 mK no magnetic phase transition was observed [203, 204]. In order to determine the low temperature nuclear orientation, samples with the radioisotope ^{141}Ce were produced by the interaction of thermal neutrons with the sample. The samples were cooled to ~10 mK and the γ-anisotropy was measured. In contrast to $CeNi_2Al_5$, no anisotropy appeared on CeNiSn, even at applied external fields [205]. Since a collapse of the energy gap was found upon doping CeNiSn, high quality crystals were grown by either the floating-zone or Czochralski methods and with different impurities. They were analyzed by metallography, electron microprobe analysis and physical measurements. The compositions of the crystals were found to be within 1% of the target composition. However, Ce_2O_3, $CeNi_2Sn_2$ and $Ce_2Ni_3Sn_2$ were detected as by-products in different ratios. The highest purity of the crystals was achieved by subsequent purification via solid-state electrotransport. In this crystal all by-products were determined to be below 0.1%. The semiconductor-like behavior found below 10 K is readily suppressed in dirty or substituted crystals, the purified sample shows metallic behavior in the resistivity along the *a* axis. This result along with the large $\gamma = 42$ mJ mol^{-1} K^{-2} supports the presence of a residual density of states at the Fermi level. Therefore the ground state of CeNiSn is not a Kondo semiconducting state, but more a semimetallic state with a pseudogap which closes along the *a* axis [80, 206]. Evidence for a quasiparticle gap in CeNiSn was generated by tunneling spectroscopy, the most direct probe to investigate the gap. The measurements were conducted using the break-junction technique with a four probe method. The energy gaps determined are nearly of the same magnitude as T_K [207]. Finally we want to mention the comparison of the thermoelectric properties of CeNiSn, CePtSn, CeRhAs, and CeRhSb [208]. All compounds are isotypic and show a δ-shaped DOS in the vicinity of the Fermi level, making them good candidates for LT thermoelectric materials. Due to the high anisotropy of these materials, the thermoelectric properties were determined along the crystallographic *b* axis. As expected, the resistivity changes from a metallic behavior in CePtSn towards a semimetallic one in CeNiSn and CeRhSb, and to a semiconducting one in CeRhAs. The opposite order is seen in the thermal conductivity κ at 290 K. While for CeRhAs an upturn in the thermal conductivity is seen below 165 K, a much weaker feature is visible for CeRhSb and CeNiSn below 20 and 15 K, respectively. Finally the Seebeck coefficient shows the same trend as the resistivity, being in line with the order of increasing Kondo temperatures T_K. As described before, the Seebeck coefficient drops to 0 for $T \rightarrow 0$ K in CeNiSn. The figure of merit zT finally represents again the strong structural anisotropy of these compounds due to large anisotropies in the trend of zT.

In heavy fermion materials the competition between RKKY and Kondo interactions causes several distinct ground states. One of these states is the so-called low carrier Kondo system, also denoted as a Kondo semiconductor [209]. Since an increase in the electrical resistivity at low temperatures was found for CeNiSn [182], CeRhAs [107], and CeRhSb [210], these three compounds were called Kondo semiconductors. The corresponding band gap energies vary from 14 K for CeNiSn to 28 K [211] for CeRhSb [211] and to 282 K for CeRhAs [35]. In the next paragraphs a large number of different gap sizes are mentioned for all three compounds depending on the measurement technique and the sample performance. Thus we would like to emphasize a publication that deals with single crystals of CeNiSn and CeRhSb with different amounts of impurities and the influence of these impurities on different physical properties [206]. The influence of the impurities and related crystallographic defects need to be considered when discussing such complex scattering effects. For instance, Ideka and Miyaka have included impurity scattering within their theory, which will be discussed later on [212].

Similar to CeNiSn, also the pnictides CeRhAs (48 entries in the SciFinder data base) [181] and CeRhSb (115 SciFinder entries) have been studied in great detail. Again, only a representative number of references can be considered herein. CeRhAs is an exceptionally good example for the importance of coherence of crystal structure and related properties. As described in the crystal structure part the lattice parameters show three anomalies ($T_1 = 370$, $T_2 = 235$

and T_3 = 165 K), which mainly concern the *a* lattice parameter. Along the *a* axis zig-zag chains of cerium are formed, and due to the structural changes the hybridization and consequently the physical properties are influenced significantly [35, 36]. Before the crystal structure had been completely understood, a gap formation has been attributed to the Kondo temperature. The gap size was determined by several methods. Evaluation of photoemission spectroscopy measurements lead to gaps of 180–200 [213] or 90–100 meV [214] below ~210 K, while transport measurements revealed a much smaller gap of 12(3) meV [215, 216]. In none of these publications the gap formation was related to structural changes. Sasakawa et al. could nicely show that the periodic lattice distortions caused by structural phase transitions influence the density of states. These are in line with the anomalies observed in the magnetic susceptibility, heat capacity, electrical resistivity, and the thermopower [35, 217]. According to this publication CeRhAs can be defined as a valence-fluctuating compound due to a broad maximum around 500 K in $\chi(T)$ and no significant anisotropic behavior can be observed. The electronic contribution to the heat capacity ($C/T = \gamma + \beta T^2 + \alpha T^3$) could be determined to γ = 3.0 mJ K^{-2}, which is one order of magnitude smaller than those reported for CeRhSb and CeNiSn. Resistivity measurements of CeRhAs have been performed with a single crystal for all three crystallographic axes. For all directions along the three principal axes, ρ(T) exhibits step-like anomalies and a significant increase can be observed below T_3. Especially, in parallel alignment to the *c* axis the three anomalies of the structural phase transitions can be observed. One peculiarity that should be mentioned is the anisotropy around the phase transitions. For instance, ρ_a jumps but ρ_c drops at T_3. Though a significant anisotropic character can be observed, all directions exhibit an increase of the electrical resistivity with lower temperatures, clearly proving a band gap in the density of states [35, 217]. Nevertheless, no ideal semiconductive behavior can be observed, most likely due to the structural distortion.

Nevertheless, the gap itself in the so-called "Kondo semiconductors" is not finally resolved and still discussed in the literature. Three different models have been discussed so far, but none of these could be established as the ideal one [36]. In contrast to the isostructural compounds CeRhSb and CeNiSn the gap formation of CeRhAs is related to lattice modulations. Already a substitution of 2.5% of As by Sb is enough to suppress all three structural phase transitions, and consequently no band gap features are observable. Hall coefficient measurements exhibited two different energy scales for the gap structure. Below T_1 a large one of 2000 K and below T_3 a small one with 300 K is reported [217]. This is accordance with optical conductivity measurements [218, 219]. By reference to detailed ^{75}As NQR/NMR data a band gap of 272 K with a band width of ≈4000 K was evaluated which is one order of magnitude larger than those in CeRhSb and CeNiSn [220]. As already reported for the antimony substitution in $CeRhSb_{1-x}As_x$, the observed structural phase transitions are intolerant to very small amounts of other elements. A similar behavior is also observed for the substitution of cerium by lanthanum according to $Ce_{1-x}La_xRhAs$. While all anomalies ascribed to the phase transition T_1 remain up to x = 0.1, no features can be observed around the temperatures of T_2 and T_3. Resistivity as well as Seebeck measurements proved that no semiconductivity is observable with x = 0.02 below T_3 [221]. The significant influence of lanthanum substitution on the Ce 4f states between x = 0.003 and 0.02 could also be shown by resonance-photoemission spectroscopy [222]. The very important influence of changes in lattice parameters on the hybridization has nicely been revealed by systematic investigations of the electrical resistivity under pressure. At 250 K the orthorhombic *b* and *c* parameters increase slightly, while the *a* parameter decreases with pressures up to 2.5 GPa [36]. In earlier publications [217] it was argued that the decrease of *a* enhances the c-f hybridization in analogy to CeNiSn, leading to the gap formation. In general it is expected that the c-f hybridization becomes stronger by applying pressure leading to an enlarged band gap. However, up to 1 GPa the activation energy increases slightly along the *c* axis, while that along the *a* axis decreases. At around 2 GPa both gap energies vanish. Consequently, discrepancies between experimental results and the simple scenario based on c-f hybridization can be ascertained [36, 223–227].

In the first publication [210], CeRhSb was classified as a valence-fluctuating compound with a rapid rise in the electrical resistivity below 21 K, which was attributed to a band gap opening in the electronic density of states with a band gap energy of about 4 K. In magnetic susceptibility studies a broad maximum at approximately 113 K, characteristic of a valence-fluctuating compound, could be observed and a fitting with the interconfiguration fluctuation (ICF) model proposed by Sales and Wohlleben led to a convincing agreement [163].

By reference to a heat capacity measurement, CeRhBi can be classified as a heavy fermion material due to the value of $\gamma \approx$ 500 mJ K^{-2} mol for the electronic contribution to the heat capacity [107]. Electrical resistivity and ^{209}Bi NQR measurements proved the absence of any magnetic ordering down to 150 mK or of a band gap opening like observed for CeRhAs and CeRhSb [18, 228]. Though no

magnetic ordering can be observed, cerium can undoubtedly be defined as Ce^{3+} according to Curie–Weiss fitting [107, 229]. The electrical resistivity of CeRhBi is almost constant down to 10 K, and on further cooling a significant drop is observed [229]. One can identify two maxima, the first one around 70 K which is very broad and flat, while the second one at 6 K is more pronounced. The latter one is taken as an onset of coherent Kondo scattering with a Kondo temperature of T_K = 9.2 K, estimated from a C_m/T vs. T plot [18]. Due to the linear temperature dependency of $\rho(T)$ below 3.5 K, CeRhBi is described as a non-Fermi liquid, which is often found in systems in the vicinity of a QCP. Different reasons for the vicinity of a QCP are listed: a $T^{-1/4}$ dependency of χ below 7 K, a change of sign in S(T) below 13 K and an increase of C/T below 8 K in proportion to –log T [229].

3.3 ^{119}Sn and ^{121}Sb Mössbauer spectroscopy

Mössbauer spectroscopic studies of the TiNiSi-type Ce*TX* phases are restricted to the stannides and antimonides. Detailed studies were performed for the series Ce*T*Sn (*T* = Ni, Pd, Pt) [49, 230, 231, 203, 232] as well as CeRhSb [89]. The ^{119}Sn spectra of the stannides reflect the single crystallographic tin site with isomer shift values in the range 1.8–2.0 mm s^{-1}. This range is close to the isomer shift values observed for the corresponding ZrNiAl-type phases [14] and various other equiatomic stannides [233]. Due to the low site symmetry of the tin atoms (*.m.*) all spectral lines are subjected to weak quadrupole splitting.

CeNiSn shows no magnetic hyperfine field splitting down to 1.5 K, while the onset of magnetic ordering (CePdSn and CePtSn order antiferromagnetically at T_N = 7.5 and 8 K) shows substantial broadening of the signals. The refined magnetic hyperfine field values were 14.5 kOe for CePdSn (at 4.2 K) [49] and 12 kOe for CePtSn (at 2 K) [230]. Results of detailed temperature dependent studies on the heavy fermion Kondo compound CePdSn clearly point to fluctuations within the antiferromagnetically ordered domains [232].

The ^{119}Sn Mössbauer spectroscopic studies were extended with respect to the hydrides $CeNiSnH_{1.0}$, $CeNiSnH_{1.8}$ [231], and CePdSnH [49]. The hydrides show similar isomer shifts as the ternary parent stannides, indicating similar s electron density at the tin nuclei. This means that the hydrogenation primarily influences the Ce–*T* bonding and thus the cerium valence. Changes in the local symmetry of the tin atoms of the hydrides are reflected by a strong increase in the quadrupole splitting parameters.

The antimonide CeRhSb and its hydride $CeRhSbH_{0.2}$ [89] show similar isomer shifts of –7.38 and –7.47 mm s^{-1}. This is the typical range for intermetallic antimonides [234, 235]. Again, the hydrogenation does not primarily affect the electronic situation of the *X* atoms, similar to the stannides.

3.4 Hydrogenation behavior

The magnetic ground state of a given Ce*TX* phase depends on the coupling constant J_{cf} between the Ce 4f and the conduction electrons. This has intensively been discussed in our previous review on the ZrNiAl-type materials [14]. The TiNiSi-type phases were also treated with hydrogen with respect to a modification of the magnetic behavior.

Hydrogenation leads to an increase in the unit cell volume. The basic crystallographic data of the Ce*TX*H_x hydrides are listed in Table 3. Only CeNiSn, CePdSn, CeRhSb, and CeIrSb form stable hydrides that keep a TiNiSi-type metal substructure, leading to CeNiSnH [47, 82, 236], CePdSnH [49], $CeRhSbH_{0.2}$ [89], and $CeIrSbH_{0.8}$ [32]. While the stannides absorb a full equivalent of hydrogen per formula unit, much smaller amounts have been observed for the antimonides. The volume incease upon hydrogen uptake is up to 4.3%.

The key question for these hydrides concerns the positions of the hydrogen atoms. Precise data has been reported for a CeNiSnD sample at 33.8 K [82]. A view of the CeNiSnD unit cell approximately along the *c* axis is presented in Fig. 5. Again, the nickel and tin atoms build a three-dimensional [NiSn] network in which the hydrogen (deuterium) atoms fill $NiCe_3$ tetrahedra. The main difference with respect to the parent stannide concerns the space group symmetry. The CeNiSnD structure was refined in the non-centrosymmetric space group $Pna2_1$, a *translationengleiche* subgroup of *Pnma*. Insertion of hydrogen leads to a violation of the mirror plane. The D@$NiCe_3$ tetrahedra share common corners, leading to chains in *c* direction.

Neutron powder diffraction data of CeNiSnD at 1.8 K shows additional reflections resulting from magnetic ordering. Ferromagnetically coupled layers extend in the *ac* plane and couple antiferromagnetically in *b* direction. This is in line with the Néel temperature of 5.1 K obtained from susceptibility measurements [82]. Thus one observes a transition from a dense Kondo system CeNiSn to a classical antiferromagnet CeNiSnD. CePdSnH [49] is isostructural to CeNiSnD. Hydrogenation leads to a decrease of the Néel temperature from 7.2 to 5.0 K.

Table 3: Lattice parameters and magnetic behavior of the hydrogenated Ce*TX* phases with orthorhombic TiNiSi-type structure (or a non-centrosymmetric variant in space group $Pna2_1$; marked with an asterisk).

Compound	*a*/pm	*b*/pm	*c*/pm	*V*/nm³	Volume increase/%	Magnetic behavior	Reference
CeNiSnD*	727.88(5)	849.74(7)	440.28(4)	0.2723	3.0	n.i.	[47]
CeNiSnD*	727.20(3)	849.51(4)	440.21(2)	0.2720	2.7	T_N = 5.1 K	[82]
$CeNiSnH_{1.8}$	727.3(3)	441.1(2)	845.8(3)	0.2713	2.6	T_C = 7.0 K	[236]
CePdSnH	741.2(2)	453.1(1)	859.3(2)	0.2886	2.5	T_N = 5.0 K	[49]
$CeRhSbH_{0.2}$	742.2(2)	462.5(2)	787.7(2)	0.2704	0.5	T_N = 3.6 K	[89]
$CeIrSbH_{0.8}$	728.16(14)	460.35(6)	825.87(2)	0.2786	4.3	<2 K	[32]

T_N, Néel temperature; T_C, Curie temperature; n.i., not investigated. The volume increase with respect to the parent compounds is also listed. For samples that did not show magnetic ordering the lowest measuring temperature is given.

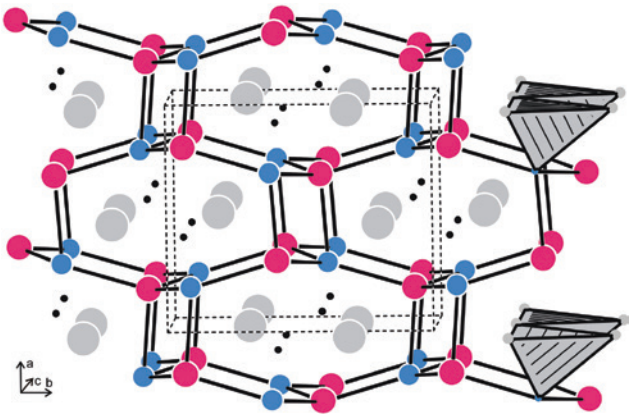

Fig. 5: The crystal structure of CeNiSnD. Cerium, nickel, tin, and deuterium atoms are drawn as medium gray, blue, magenta, and black circles, respectively. The three-dimensional [NiSn] network and some D@$NiCe_3$ tetrahedra are emphasized.

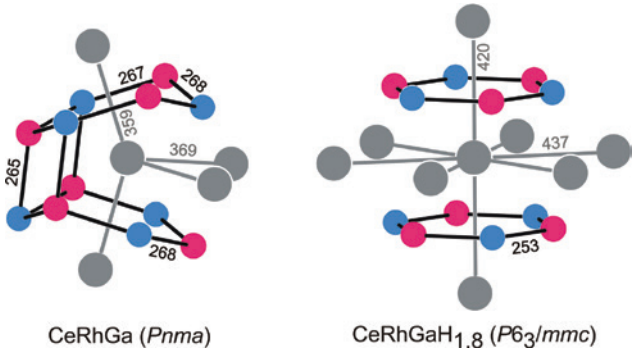

Fig. 6: Coordination of the cerium atoms in the structures of CeRhGa and $CeRhGaH_{1.8}$. Cerium, thodium, and gallium atoms are drawn as medium gray, blue, and magenta circles, respectively. The Rh_3Ga_3 hexagons are emphasized.

The pressure dependence of magnetic ordering was studied for CeNiSnH and $CeNiSnH_{1.8}$ in a CuBe piston-cylinder pressure cell [237]. The Néel temperature of CeNiSnH increases with increasing pressure from 4.77 to 5.01 K, while the Curie temperature of the hydrogen-rich hydride $CeNiSnH_{1.8}$ decreases from 7.16 to 5.30 K.

Hydrogenation of the intermediate valent antimonide CeIrSb ends at a composition $CeIrSbH_{0.8}$ [32]. Consequently, the hydrogen sites are only partially filled. Although this induces some kind of structural disorder, the magnetic ground state switches to antiferromagnetic with T_N = 7.0 K. The antiferromagnetic ground state has also been manifested by ab initio electronic structure calculations [104]. CeRhSb absorbs up to 0.2 hydrogen atoms per formula unit [89]. The amount of hydrogen was carefully analyzed by a combustion analyses. Again, hydrogenation induces a switch from the Kondo semiconductor CeRhSb to the antiferromagnetic hydride $CeRhSbH_{0.2}$ (T_N = 3.6 K) [89]. This antiferromagnetic ground state is also underlined by a spin-flip transition around 10 kOe.

Hydrogenation of CeNiSn with large hydrogen quantities leads to the hydrogen-rich hydride $CeNiSnH_{1.8}$ [236] which shows a drastic change in the metal substructure, similar to CeIrAl [56], CeAuAl [238], CeRhGa, CeIrGa [67, 71], CeRhGe, CeIrGe [239], CeNiGa [63, 240], and CeCuGa [241]. As an example we present the structures of CeRhGa and $CeRhGaH_{1.8}$ in Fig. 6. The strongly puckered Rh_3Ga_3 hexagons of the parent gallide CeRhGa become planar in $CeRhGaH_{1.8}$ (this metal substructure corresponds to the ZrBeSi type [95]). Again, the hydrogen atoms fill $RhCe_3$ tetrahedral voids between cerium and [RhGa] layers. The planarity of the Rh_3Ga_3 hexagons and the absence of interlayer Rh–Ga bonding increase the number of tetrahedral sites by a factor of 2 and the maximum hydrogen content can reach Ce*TX*H_2.

For the hydrides of CeNiGa and CeCuGa, only the AlB_2 subcell has been reported. This might be a consequence of the similar scattering powers of the pairs Ni/Ga and Cu/Ga which leads to very weak intensities of the superstructure reflections.

3.5 Solid solutions

Besides the detailed magnetic and transport studies of the pure Ce*TX* compounds, in an extension of the work, a huge number of solid solutions has been prepared in order to investigate changes in the magnetic ground state as a function of the VEC. Similar to the ZrNiAl-type materials [14], the cerium, the transition metal, and the atoms on the *X* sites have been substituted systematically.

Our summary starts with the substitutions on the cerium site. These studies mainly focus on Ce/La substitution, diluting the *RE* magnetic substructure through incorporation of diamagnetic La^{3+}. The solid solution $Ce_{1-x}La_xNiSn$ [242–244] shows almost Vegard-type behavior for the lattice parameters and one observes a crossover from a Kondo insulator (CeNiSn) to a single-ion Kondo ground state (for a lanthanum concentration larger than 20%). The reduction of the magnetic correlations has been independently confirmed by myon spin-rotation relaxation [244]. Results of parallel resistivity measurements on $Ce_{0.2}La_{0.8}PdSn$ have underlined that the parent stannide CePdSn is a dense Kondo compound [153].

The arsenide CeRhAs has been substituted only with small amounts of lanthanum up to a maximum concentration of $Ce_{0.95}La_{0.05}RhAs$ [221, 222, 245]. These samples were studied by high-resolution resonance-photoemission spectroscopy in order to explain the collapse of the energy gap in the Kondo semiconducting state of CeRhAs as a consequence of cerium-by-lanthanum substitution. This response could also be detected for the resistivity through break-junction tunneling experiments [221]. With the heavier congener antimony, Vegard-type behavior occurs for the solid solution $Ce_{1-x}La_xRhSb$ [242]. The gap formation observed for the parent antimonide CeRhSb is already suppressed at a very low level of Ce/La substitution. These studies have underlined that a coherent Kondo state is essential for gap formation in CeRhSb [87]. A further interesting result concerns the lanthanum-rich part of the solid solution. Superconductivity in LaRhSb (T_C ~ 2.5 K) is suppressed at low levels of La/Ce substitution. In between one observes a gradual change from intermediate cerium valence to Curie–Weiss behavior with increasing *x*. The Kondo hole state in the solid solution $Ce_{1-x}La_xRhSb$ was verified through a detailed study by photoelectron spectroscopy [246]. The low-temperature semiconducting state of CeRhSb already disappears at a composition $Ce_{0.8}La_{0.2}RhSb$ [247]. μSR studies have shown that the magnetic ground state in the solid solution $Ce_{1-x}La_xRhSb$ does not alter significantly up to $x \approx 0.1$ [248].

Similar data has been collected for the solid solution $Ce_{1-x}La_xPtGa$ [249]. The course of the three lattice parameters shows Vegard-type behavior. With increasing lanthanum concentration one observes lowering of the Néel temperature which starts at T_N = 3.3 K for CePtGa. This shift also became evident in resistivity measurements which show pronounced Kondo-type minima.

The last point of the cerium substitution concerns substitution with an actinoid atom. Besides diamagnetic lanthanum it is also possible to substitute with diamagnetic Th^{4+} [250, 251]. Up to 60% of the cerium atoms can be substituted by thorium in the solid solution $Ce_{1-x}Th_xRhSb$. Besides the dilution of the cerium magnetic moments, tetravalent thorium also leads to an increase of the VEC. The thorium substitution induces non-Fermi liquid behavior. Cerium–uranium substitution has been tested for $Ce_{1-x}U_xNiSn$ [252–254]. Samples with up to 30% uranium were prepared. The gap formed at low temperatures for the Kondo insulator CeNiSn is already destroyed at small uranium substitutions. The Ce/U mixing leads to an inhomogeneously ordered magnetic state. μSR data point to a coexistence of magnetically ordered domains along with paramagnetic ones.

The broadest investigations were performed for solid solutions on the transition metal position. A highly interesting situation concerns the solid solution $CeRh_{1-x}Ir_xGe$ [76, 166, 255] combining the antiferromagnet CeRhGe and the intermediate valence compound CeIrGe. The change of the cerium valence state between the two ternaries is also manifested for the solid solution. Magnetic susceptibility studies at 300 and 77 K have shown a pronounced anomaly in the susceptibility around $x \approx 0.3$ [166]. In a subsequent study a sample of composition $CeRh_{0.69}Ir_{0.31}Ge$ [76] was characterized as a function of temperature. A first order cerium valence transition takes place in the temperature interval 236–258 K, thus exhibiting pronounced hysteresis. The $[Rh_{0.69}Ir_{0.31}Ge]$ polyanionic network changes its puckering as a function of temperature. This phase transition is similar to that between LT- und HT-CeRhGe described above [77].

The most prominent TiNiSi-type Ce*TX* phase is CeNiSn (*vide ultra*), and consequently many solid solutions have been prepared for this stannide. The first two series concern solid solutions with the same valence electron concentration. The nickel atoms in CeNiSn have been substituted by palladium [199, 256, 257] and platinum [258–264]. In the solid solution $CeNi_{1-x}Pd_xSn$ one observes a decrease of the Néel temperature of CePdSn from 7.5 K to around 4 K for a composition $CeNi_{0.4}Pd_{0.6}Sn$ [256]. The transport properties show a change from a semiconducting-like Kondo state to a metal with increasing palladium concentration. These trends are underlined by electronic structure studies on the basis of photoemission spectroscopy [257].

The platinum-based solid solution $CeNi_{1-x}Pt_xSn$ shows almost Vegard-type behavior in its lattice parameters [258]. Antiferromagnetic ordering arises from a composition $CeNi_{0.6}Pt_{0.4}Sn$. This is evident from magnetic susceptibility as well as specific heat data. Resistivity data shows an increasing strength of the Kondo effect with increasing nickel content, and μSR data shows only a tiny influence of platinum substitution on the myon spin relaxation rate [261, 262]. Finally the solid solution between the stannides CePdSn and CePtSn was tested [265]. A single crystal of composition $CePt_{0.75}Pd_{0.25}Sn$ was grown with a modified Czochralski method. Specific heat data showed multiple magnetic phase transitions at low temperature. The main problem arising in the study of this solid solution is the segregation of the samples into domains with different compositions (cluster formation), hampering precise property studies.

Substitution of nickel by cobalt leads to a decrease of the VEC [266–273]. Samples were prepared up to a composition $CeNi_{1-x}Co_xSn$ with $x = 0.5$ in polycrystalline as well as in single crystalline form (Czochralski technique along with inductive heating). Increasing cobalt content leads to a moderate increase of the unit cell volume. The cobalt substitution readily leads to a closing of the gap in the density of states at low temperatures, which can also be monitored through thermal conductivity measurements [270]. In the x range from 0.35 to 0.40 a first order valence phase transition takes place. The transition temperature changes from 40 to 80 K as a function of the cobalt concentration [267]. In the regime with lower cobalt content typical valence fluctuation behavior is observed. The strong correlation between the antiferromagnetic properties and the pseudo-gap formation was manifested by single crystal neutron scattering experiments for a crystal of composition $CeNi_{0.9}Co_{0.1}Sn$ [268, 269]. The valence phase transition was also tested by ^{119}Sn and ^{59}Co solid state NMR spectroscopy for a sample of composition $CeNi_{0.65}Co_{0.35}Sn$ [273]. The quadrupole frequency for ^{59}Co shows a strong anomaly around the phase transition temperature, similar to the spin-lattice relaxation time detected for ^{119}Sn.

The TiNiSi type is stable for the solid solution $CeNi_{1-x}Rh_xSn$ up to ≈0.7 and then switches to the ZrNiAl-type structure. The Ni/Rh substitution was studied in detail with respect to the influence on the gap formation in CeNiSn [274–277]. Already a low degree of rhodium substitution induces structural disorder which turns the solid solution into a glassy state (magnetic disorder) and then switches to non-Fermi liquid behavior [275]. Detailed magnetic susceptibility and specific heat studies and considerations of the change in VEC yielded a magnetic mean-field phase diagram (hybridization as a function of the number of valence electrons).

Gap suppression in CeNiSn is also possible through an increase of the VEC. The solid solution $CeNi_{1-x}Cu_xSn$ keeps the TiNiSi type up to ≈0.3 [278–282]. Increasing copper content leads to an increase of the density-of-states at the Fermi level. The magnetic correlations in $CeNi_{1-x}Cu_xSn$ were additionally studied by μSR as well as pulsed and continuous myon beam techniques [280]. A Czochralski grown crystal of composition $CeNi_{0.87}Cu_{0.13}Sn$ was studied by high-resolution magnetic neutron spectroscopy. The copper substitution induces long-range antiferromagnetic order below $T_N = 1.4$ K for the compound $CeNi_{0.87}Cu_{0.13}Sn$ with a commensurate wave vector (0 1/2 0) [281]. Similar results were obtained in a parallel study by temperature dependent susceptibility and specific heat studies on a $CeNi_{0.82}Cu_{0.18}Sn$ single crystal which showed a slightly higher Néel temperature of 3.5 K [282]. The susceptibility studies allowed for a construction of the magnetic phase diagram and a determination of the crystal field level splitting energies of $\Delta_1 = 320$ and $\Delta_2 = 467$ K.

The following solid solutions concern the modification of the physical properties of CeRhSb. Up to 30% of the rhodium atoms were substituted by nickel or palladium [209, 283–286]. These samples were structurally studied in the broad temperature range from 10 to 300 K. X-ray powder diffraction data is in agreement with an almost isotropic expansion of the unit cells with increasing temperature. There were no hints for structural phase transitions in the studied temperature range. The nickel and palladium substitution gradually shifts the cerium f shell to a $4f^1$ state along with a suppression of the gap, similar to the situation discussed for CeNiSn. The ground state of the Ce^{3+} ion was studied for samples of compositions $CeRh_{0.9}Pd_{0.1}Sb$ and $CeRh_{0.8}Pd_{0.2}Sb$ with the help of inelastic neutron scattering [209]. Specific heat data of $CeRh_{0.7}Pd_{0.3}Sb$ indicates antiferromagnetic ordering at 2.5 K. The occurrence of magnetic ordering within this solid solution readily reminds of the hydride $CeRhSbH_{0.2}$ [89] discussed above.

Magnetic ordering was studied for the solid solution $CePt_{1-x}Pd_xAl$ for x values ranging from 0.1 to 0.8 [287]. Multi-phased samples were observed for larger x values with contributions of a ZrNiAl-type phase. The samples with low palladium content reveal ferromagnetic ordering of the cerium magnetic moments followed by a switch to an antiferromagnetic ground state with increasing x. This antiferromagnetic ground state is underlined for the x = 0.2–0.7 samples through metamagnetic transitions.

The corresponding solid solution with gallium was studied for the whole concentration range [288]. The

lattice parameters and the magnetic ordering temperature behave in a Vegard-type manner. T_N decreases from 3.4 K (CePtGa) to 1.3 K (CePdGa). The antiferromagnetic transitions are well resolved in susceptibility and specific heat measurements. Similar behavior was found for the solid solution $CePt_{1-x}Ni_xGa$ [289]. Further substitution experiments concerned $CePtGa_{1-x}Al_x$.

The last three solid solutions concern the intermediate valence compounds CeRuSn [290] and CeRhSn [291]. Samples of $CeRu_{1-x}Pd_xSn$ and $CeRh_{1-x}Pd_xSn$ [292] adopt the TiNiSi type only for $x > 0.85$. These samples all show stable trivalent cerium. A similar situation occurs for $CeRu_{1-x}Ni_xSn$ [293] where the TiNiSi type is stable for $x > 0.6$, again with trivalent cerium.

Finally we turn to solid solutions with substitutions on the *X* site. The broadest studies were carried out for $CeRhSb_{1-x}Sn_x$ [294–297]. The TiNiSi-type structure is only stable for low concentrations of tin ($x < 0.2$). The Kondo gap readily disappears by tin substitution and the solid solution switches to a non-Fermi liquid system. The low-temperature behavior of the solid solution $CeRhSb_{1-x}Sn_x$ has been reviewed along with $Ce_{1-x}La_xRhSn$ [298]. One of the decisive influences leading to a suppression of the Kondo gap is the carrier concentration which can effectively be changed through variation of the valence electron concentration, i.e. substitution of antimony by a group IV element. This has also been tested for the more complex solid solutions $CeNi_{1-\delta}Sn_{1+\delta-x}Sb_x$ [299] and $CeRhSb_{1-x}Te_x$ [300].

The interplay of crystal and electronic structure on the gap formation in CeRhAs and CeRhSb was also studied for several compositions of the solid solution $CeRhAs_{1-x}Sb_x$ [217]. The structural behavior of these samples was investigated by temperature dependent powder X-ray diffraction, revealing diverse anomalies, and there were hints for modulations and orthorhombic/hexagonal phase transitions.

The last solid solution draws back to the stannide CeNiSn [301–303]. The tin atoms can stepwise be substituted by germanium, leading to a crossover from Kondo lattice to valence fluctuation behavior.

4 Summary

The different facets of magnetic ground states in TiNiSi-type Ce*TX* intermetallics are reviewed and some structure-property relationships have been elucidated. Tuning of the physical properties of these Ce*TX* intermetallics is possible through application of external pressure, through the formation of solid solutions (geometrical and electronic influence) or by hydrogenation reactions. Our critical literature survey shows that the broad field of cerium intermetallics still plays an important role in condensed matter physics and chemistry.

Acknowledgments: This work was supported by the Deutsche Forschungsgemeinschaft. O. N. is indebted to the NRW Forschungsschule “Molecules and Materials – A Common Design Principle” for a PhD fellowship.

References

[1] P. Villars, K. Cenzual, *Pearson’s Crystal Data: Crystal Structure Database for Inorganic Compounds* (release 2014/15), ASM International®, Materials Park, Ohio (USA) **2014**.
[2] A. Szytuła, J. Leciejewicz, *Handbook of Crystal Structures and Magnetic Properties of Rare Earth Intermetallics*, CRC Press, Boca Raton, **1994**.
[3] B. Coqblin, M. A. Gusmão, J. R. Iglesias, C. Lacroix, S. G. Magalhães, A. Ruppenthal, A. A. Schmidt, A. Theumann, *The Kondo-Lattice Model for Cerium Compounds*, in *Electron Correlations and Materials Properties 2*, (Eds.: A. Gonis, N. Kioussis, M. Ciftan), Kluwer Academic Publishers, New York, **2002**, p. 159.
[4] G. R. Stewart, *Rev. Mod. Phys*. **2006**, *78*, 743.
[5] R. Settai, T. Takeuchi, Y. Ōnuki, *J. Phys. Soc. Jpn*. **2007**, *76*, 051003.
[6] H. von Löhneysen, A. Rosch, M. Vojta, P. Wölfle, *Rev. Mod. Phys*. **2007**, *79*, 1015.
[7] O. Stockert, S. Kirchner, F. Steglich, Q. Si, *J. Phys. Soc. Jpn*. **2012**, *81*, 011001.
[8] S. F. Matar, *Progr. Solid State Chem*. **2013**, *41*, 55.
[9] S. Gupta, K. G. Suresh, *J. Alloys Compd*. **2015**, *618*, 562.
[10] P. I. Krypyakevich, V. Ya. Markiv, E. V. Melnyk, *Dopov. Akad. Nauk. Ukr. RSR Ser. A* **1967**, 750.
[11] A. E. Dwight, M. H. Mueller, R. A. Conner Jr., J. W. Downey, H. Knott, *Trans. Met. Soc. AIME* **1968**, *242*, 2075.
[12] M. F. Zumdick, R.-D. Hoffmann, R. Pöttgen, *Z. Naturforsch*. **1999**, *54b*, 45.
[13] C. B. Shoemaker, D. P. Shoemaker, *Acta Crystallogr*. **1965**, *18*, 900.
[14] R. Pöttgen, B. Chevalier, *Z. Naturforsch*. **2015**, *70b*, 289.
[15] R. Pöttgen, Th. Gulden, A. Simon, *GIT Labor-Fachzeitschrift* **1999**, *43*, 133.
[16] H. Kitazawa, A. Dönni, L. Keller, J. Tang, F. Fauth, G. Kido, *J. Solid State Chem*. **1998**, *140*, 233.
[17] P. Salamakha, O. Sologub, T. Suemitsu, T. Takabatake, *J. Alloys Compd*. **2000**, *313*, L5.
[18] S. Yoshii, D. Tazawa, M. Kasaya, *Physica B* **1997**, *230–233*, 380.
[19] R. Pöttgen, D. Johrendt, *Intermetallics*, De Gruyter, Berlin, **2014**.
[20] R. Mishra, W. Hermes, R. Pöttgen, *Z. Naturforsch*. **2007**, *62b*, 1581.
[21] S. K. Dhar, R. Kulkarni, H. Hidaka, Y. Toda, H. Kotegawa, T. C. Kobayashi, P. Manfrinetti, A. Provino, *J. Phys.: Condens. Matter* **2009**, *21*, 156001.

[22] J. Emsley, *The Elements*, Oxford University Press, Oxford **1999**.
[23] J. D. Corbett, A. Simon, *Inorg. Synth*. **1983**, *22*, 15.
[24] D. Kußmann, R.-D. Hoffmann, R. Pöttgen, *Z. Anorg. Allg. Chem*. **1998**, *624*, 1727.
[25] R. Pöttgen, A. Lang, R.-D. Hoffmann, B. Künnen, G. Kotzyba, R. Müllmann, B. D. Mosel, C. Rosenhahn, *Z. Kristallogr*. **1999**, *214*, 143.
[26] P. Lemoine, A. Vernière, J. F. Marêché, B. Malaman, *J. Alloys Compd*. **2010**, *508*, 9.
[27] P. Manfrinetti, A. Provino, K. A. Gschneidner Jr., *J. Alloys Compd*. **2009**, *482*, 81.
[28] D. Rossi, R. Ferro, *J. Alloys Compd*. **2001**, *317–318*, 521.
[29] D. Rossi, R. Marazza, R. Ferro, *J. Less-Common Met*. **1985**, *107*, 99.
[30] P. Rogl, B. Chevalier, M. J. Besnus, J. Etourneau, *J. Magn. Magn. Mater*. **1989**, *80*, 305.
[31] D. Niepmann, Yu. M. Prots', R. Pöttgen, W. Jeitschko, *J. Solid State Chem*. **2000**, *154*, 329.
[32] E. Gaudin, B. Chevalier, W. Hermes, U. Ch. Rodewald, R. Pöttgen, *J. Solid State Chem*. **2009**, *182*, 1827.
[33] H. Kitazawa, S. Nimori, J. Tang, F. Iga, A. Dönni, T. Matsumoto, G. Kido, *Physica B* **1997**, *237–238*, 212.
[34] T. Ueda, H. Harima, T. Yasuda, T. Kawai, R. Settai, Y. Ōnuki, *J. Magn. Magn. Mater*. **2007**, *310*, 391.
[35] T. Sasakawa, T. Suemitsu, T. Takabatake, Y. Bando, K. Uemo, M. H. Jung, M. Sera, T. Suzuki, T. Fujita, M. Nakajima, K. Iwasa, M. Kohgi, Ch. Paul, St. Berger, E. Bauer, *Phys. Rev. B* **2002**, *66*, 041103.
[36] K. Uemo, K. Masumori, T. Sasakawa, F. Iga, T. Takabatake, Y. Ohishi, T. Adachi, *Phys. Rev. B* **2005**, *71*, 064110.
[37] J. F. Riecken, G. Heymann, W. Hermes, U. Ch. Rodewald, R.-D. Hoffmann, H. Huppertz, R. Pöttgen, *Z. Naturforsch*. **2008**, *63b*, 695.
[38] G. Heymann, J. F. Riecken, S. Rayaprol, S. Christian, R. Pöttgen, H. Huppertz, *Z. Anorg. Allg. Chem*. **2007**, *633*, 77.
[39] J. F. Riecken, G. Heymann, T. Soltner, R.-D. Hoffmann, H. Huppertz, D. Johrendt, R. Pöttgen, *Z. Naturforsch*. **2005**, *60b*, 821.
[40] H. Huppertz, *Z. Kristallogr.* **2004**, *219*, 330.
[41] D. Walker, M. A. Carpenter, C. M. Hitch, *Am. Mineral.* **1990**, *75*, 1020.
[42] D. Walker, *Am. Mineral.* **1991**, *76*, 1092.
[43] D. C. Rubie, *Phase Trans.* **1999**, *68*, 431.
[44] R. Pöttgen, H. Borrmann, R. K. Kremer, *J. Magn. Magn. Mater*. **1996**, *152*, 196.
[45] V. Brouskov, M. Hanfland, R. Pöttgen, U. Schwarz, *Z. Kristallogr*. **2005**, *220*, 122.
[46] B. Chevalier, M. Pasturel, J.-L. Bobet, R. Decourt, J. Etourneau, O. Isnard, J. Sanchez Marcos, J. Rodriguez Fernandez, *J. Alloys Compd*. **2004**, *383*, 4.
[47] M. Stange, V. Paul-Boncour, M. Latroche, A. Percheron-Guégan, O. Isnard, V. A. Yartys, *J. Alloys Compd*. **2005**, *404–406*, 144.
[48] J.-L. Bobet, M. Pasturel, B. Chevalier, *Intermetallics* **2006**, *14*, 544.
[49] B. Chevalier, A. Wattiaux, J.-L. Bobet, *J. Phys.: Condens. Matter* **2006**, *18*, 1743.
[50] C. Ritter, A. Provino, P. Manfrinetti, K. A. Gschneidner Jr., *J. Alloys Compd*. **2011**, *509*, 9724.
[51] M. L. Fornasini, A. Iandelli, F. Merlo, M. Pani, *Intermetallics* **2000**, *8*, 239.
[52] W. Hermes, R. Mishra, H. Müller, D. Johrendt, R. Pöttgen, *Z. Anorg. Allg. Chem*. **2009**, *635*, 660.
[53] A. Iandelli, *J. Less-Common Met*. **1991**, *169*, 187.
[54] A. Ślebarski, D. Kaczorowski, W. Głogowski, J. Goraus, *J. Phys.: Condens. Matter* **2008**, *20*, 315208.
[55] F. Hulliger, *J. Alloys Compd*. **1995**, *229*, 265.
[56] S. K. Malik, P. Raj, A. Sathyamoorthy, K. Shashikala, N. Harish Kumar, L. Menon, *Phys. Rev. B* **2001**, *63*, 172418.
[57] N. Harish Kumar, L. Menon, C. R. Venkateswara Rao, S. K. Malik, P. Raj, A. Sathyamoorthy, K. Shashikala, *Solid State Commun*. **1999**, *109*, 345.
[58] F. Hulliger, *J. Alloys Compd*. **1993**, *196*, 225.
[59] B. Xue, H. Schwer, *J. Alloys Compd*. **1994**, *204*, L25.
[60] J.-L. Bobet, B. Chevalier, F. Weill, J. Etourneau, *J. Alloys Compd*. **2002**, *330–332*, 373.
[61] F. Hulliger, *J. Alloys Compd*. **1993**, *200*, 75.
[62] L. Menon, S. K. Malik, *Phys. Rev. B* **1995**, *51*, 5858.
[63] B. Chevalier, J.-L. Bobet, E. Gaudin, M. Pasturel, J. Etourneau, *J. Solid State Chem*. **2002**, *168*, 28.
[64] V. Y. Markiv, N. N. Belyavina, T. I. Zhunkovskaya, *Dopov. Akad. Nauk Ukr. RSR, Ser. A* **1982**, *2*, 80.
[65] W. Hermes, R. Mishra, U. Ch. Rodewald, R. Pöttgen, *Z. Naturforsch*. **2008**, *63b*, 537.
[66] J. Goraus, A. Ślebarski, M. Fijałkowski, *J. Alloys Compd*. **2011**, *509*, 3735.
[67] B. Chevalier, B. Heying, U. Ch. Rodewald, C. P. Sebastian, E. Bauer, R. Pöttgen, *Chem. Mater*. **2007**, *19*, 3052.
[68] F. Hulliger, *J. Alloys Compd*. **1996**, *239*, 131.
[69] E. Hovestreydt, N. Engel, K. Klepp, B. Chabot, E. Parthé, *J. Less-Common Met*. **1982**, *85*, 247.
[70] J. Goraus, A. Ślebarski, M. Fijałkowski, Ł. Hawełek, *Eur. Phys. J. B* **2011**, *80*, 65.
[71] P. Raj, A. Sathyamoorthy, K. Shashikala, C. R. Venkateswara Rao, S. K. Malik, *Solid State Commun*. **2001**, *120*, 375.
[72] Yu. D. Seropegin, B. I. Shapiev, A. V. Gribanov, O. I. Bodak, *J. Alloys Compd*. **1999**, *288*, 147.
[73] P. Salamakha, M. Konyk, O. Sologub, O. Bodak, *J. Alloys Compd*. **1996**, *236*, 206.
[74] B. Chevalier, M. Pasturel, J.-L. Bobet, F. Weill, R. Decourt, J. Etourneau, *J. Solid State Chem*. **2004**, *177*, 752.
[75] Yu. D. Seropegin, A. V. Gribanov, O. I. Bodak, *J. Alloys Compd*. **1998**, *269*, 157.
[76] E. Gaudin, B. Chevalier, B. Heying, U. Ch. Rodewald, R. Pöttgen, *Chem. Mater*. **2005**, *17*, 2693.
[77] V. Svitlyk, W. Hermes, B. Chevalier, S. F. Matar, E. Gaudin, D. Voßwinkel, D. Chernyshov, R.-D. Hoffmann, R. Pöttgen, *Solid State Sci*. **2013**, *21*, 6.
[78] A. V. Gribanov, Y. D. Seropegin, O. I. Bodak, V. N. Nikiforov, A. A. Velikhovskii, J. Mirkovic, *J. Phase Eq*. **1996**, *17*, 196.
[79] R. V. Skolozdra, L. P. Komarovskaya, *Izv. Akad. Nauk. SSSR, Met*. **1988**, *2*, 214.
[80] G. Nakamoto, T. Takabatake, H. Fujii, A. Minami, K. Maezawa, I. Oguro, A. A. Menovsky, *J. Phys. Soc. Jpn*. **1995**, *64*, 4834.
[81] A. Hiess, I. Zobkalo, M. Bonnet, J. Schweizer, E. Lelièvre-Berna, F. Tasset, Y. Isikawa, G. H. Lander, *J. Phys.: Condens. Matter* **1997**, *9*, 9321.
[82] V. A. Yartys; B. Ouladdiaf, O. Isnard, O. Yu. Khyzhun, K. H. J. Buschow, *J. Alloys Compd*. **2003**, *359*, 62.
[83] I. Higashi, K. Kobayashi, T. Takabatake, M. Kasaya, *J. Alloys Compd*. **1993**, *193*, 300.

[84] D. T. Adroja, S. K. Malik, *Phys. Rev. B* **1992**, *45*, 779.
[85] S. Nakamura, T. Goto, Y. Isikawa, S. Sakatsume, M. Kasaya, *J. Phys. Soc. Jpn*. **1991**, *60*, 2305.
[86] A. Zygmunt, A. Szytuła, *J. Alloys Compd*. **1995**, *219*, 185.
[87] S. K. Malik, L. Menon, K. Gosh, S. Ramakrishnan, *Phys. Rev. B* **1995**, *51*, 399.
[88] M. G. Haase, T. Schmidt, C. G. Richter, H. Block, W. Jeitschko, *J. Solid State Chem*. **2002**, *168*, 18.
[89] B. Chevalier, R. Decourt, B. Heying, F. M. Schappacher, U. Ch. Rodewald, R.-D. Hoffmann, R. Pöttgen, R. Eger, A. Simon, *Chem. Mater*. **2007**, *19*, 28.
[90] H. Bärnighausen, *Commun. Math. Chem*. **1980**, *9*, 139.
[91] U. Müller, *Z. Anorg. Allg. Chem*. **2004**, *630*, 1519.
[92] U. Müller, *Relating crystal structures by group-subgroup relations*, in *International Tables for Crystallography*, Vol. A1, *Symmetry relations between space groups*, 2nd edition, (Eds.: H. Wondratschek, U. Müller), John Wiley & sons, Ltd, Chichester, **2010**, p. 44.
[93] U. Müller, *Symmetriebeziehungen zwischen verwandten Kristallstrukturen*, Vieweg + Teubner Verlag, Wiesbaden, **2012**.
[94] E. J. Duwell, N. C. Baenziger, *Acta Crystallogr*. **1955**, *8*, 705.
[95] R.-D. Hoffmann, R. Pöttgen, *Z. Kristallogr*. **2001**, *216*, 127.
[96] R. Pöttgen, *Z. Anorg. Allg. Chem*. **2014**, *640*, 869.
[97] G. Nuspl, K. Polborn, J. Evers, G. A. Landrum, R. Hoffmann, *Inorg. Chem*. **1996**, *35*, 6922.
[98] G. A. Landrum, R. Hoffmann, J. Evers, H. Boysen, *Inorg. Chem*. **1998**, *37*, 5754.
[99] E. Parthé, L. Gelato, B. Chabot, M. Penzo, K. Cenzual, R. Gladyshevskii, TYPIX-*Standardized Data and Crystal Chemical Characterization of Inorganic Structure Types*, *Gmelin Handbook of Inorganic and Organometallic Chemistry*, 8th ed., Springer, Berlin **1993**.
[100] M. D. Bojin, R. Hoffmann, *Helv. Chim. Acta* **2003**, *86*, 1653.
[101] M. D. Bojin, R. Hoffmann, *Helv. Chim. Acta* **2003**, *86*, 1683.
[102] S. F. Matar, E. Gaudin, B. Chevalier, R. Pöttgen, *Solid State Sci*. **2007**, *9*, 274.
[103] S. F. Matar, A. F. Al Alam, M. Nakhl, R. Pöttgen, B. Chevalier, N. Quaini, *Solid State Sci*. **2011**, *13*, 1704.
[104] S. F. Matar, E. Gaudin, B. Chevalier, R. Pöttgen, *Solid State Sci*. **2011**, *13*, 948.
[105] J. Donohue, *The Structures of the Elements*, Wiley, New York, **1974**.
[106] H. H. Hill, in *Plutonium and Other Actinides, Nuclear Materials Series, AIME*, (Ed.: W. N. Mines), **1970**, *17*, 2.
[107] S. Yoshii, M. Kasaya, H. Takahashi, N. Mori, *Physica B* **1996**, *223&224*, 421.
[108] M. Nakajima, K. Iwasa, M. Kohgi, T. Sasakawa, T. Takabatake, *Acta Phys. Polon. B* **2003**, *34*, 1109.
[109] C. Schank, F. Jährling, L. Luo, A. Grauel, C. Wassilew, R. Borth, G. Olesch, C. D. Bredl, C. Geibel, F. Steglich, *J. Alloys Compd*. **1994**, *207/208*, 329.
[110] Yu. M. Prots', R. Pöttgen, D. Niepmann, M. W. Wolff, W. Jeitschko, *J. Solid State Chem*. **1999**, *142*, 400.
[111] Yu. M. Prots', R. Pöttgen, W. Jeitschko, *Z. Anorg. Allg. Chem*. **1998**, *624*, 425.
[112] F. C. Ragel, P. de V. du Plessis, A. M. Strydom, *J. Phys.: Condens. Matter* **2007**, *19*, 506211.
[113] M. Shirakawa, M. Kasaya, Y. Uwatoko, G. Oomi, N. Môri, *Physica B* **2000**, *281&282*, 94.
[114] H.-M. Hou, D. Jin, Y.-P. Wang, J.-L. Luo, E. Nyeanchi, D. F. Brewer, A. L. Thomson, *Chin. Phys. Lett*. **1998**, *15*, 62.
[115] J. Goraus, A. Ślebarski, M. Fijałkowski, *Phys. Stat. Sol*. **2011**, *248*, 2857.
[116] K. G. Suresh, S. K. Dhar, A. K. Nigam, *J. Magn. Magn. Mater*. **2005**, *288*, 452.
[117] S. K. Dhar, Y. Aoki, B. Suemitsu, R. Miyazaki, A. Provino, P. Manfrinetti, *J. Appl. Phys*. **2014**, *115*, 17E113.
[118] S. Doniach, *Physica* **1977**, *91B*, 231.
[119] J. R. Iglesias, C. Lacroix, B. Coqblin, *Phys. Rev. B* **1997**, *56*, 11820.
[120] Y.-F. Yang, Z. Fisk, H.-O. Lee, J. D. Thompson, D. Pines, *Nature* **2008**, *454*, 611.
[121] A. Dönni, H. Kitazawa, P. Fischer, J. Tang, M. Kohgi, Y. Endoh, Y. Morii, *J. Phys.: Condens. Matter* **1995**, *7*, 1663–1678.
[122] Y.-S. Li, Y. Lu, Q.-F. Lu, *J. Jiangxi Normal Univ. (Nat. Sci.)* **2006**, *30*, 532.
[123] T. Ueda, M. Nakashima, M. Hedo, Y. Uwatoko, H. Nakashima, A. Thamizhavel, T. D. Matsuda, Y. Haga, R. Settai, Y. Ōnuki, *J. Phys. Soc. Jpn*. **2005**, *74*, 3393.
[124] T. Ueda, M. Nakashima, H. Nakashima, A. Thamizhavel, M. Hedo, Y. Uwatoko, T. D. Matsuda, Y. Haga, R. Settai, Y. Ōnuki, *Physica B* **2006**, *378–380*, 801.
[125] M. Nakashima, T. Ueda, K. Shimizu, H. Nakashima, A. Thamizhavel, N. Tateiwa, Y. Haga, M. Hedo, Y. Uwatoko, R. Settai, Y. Ōnuki, K. Izawa, G. Knebel, B. Salce, J. Flouquet, *J. Magn. Magn. Mater*. **2007**, *310*, e9.
[126] D. T. Adroja, B. D. Rainford, S. K. Malik, *Physica B* **1993**, *186–188*, 566.
[127] J. A. Mydosh, *J. Magn. Magn. Mater.* **1996**, *157/158*, 606.
[128] K. Binder, A. P. Young, *Rev. Mod. Phys*. **1986**, *58*, 801.
[129] J. Kondo, *Prog. Theor. Phys*. **1964**, *32*, 37.
[130] P. Lemoine, A. Vernière, G. Venturini, S. Capelli, B. Malaman, *J. Magn. Magn. Mater*. **2012**, *324*, 961.
[131] L. Menon, S. K. Dhar, S. K. Malik, *Physica B*, **1996**, *223&224*, 283.
[132] D. T. Adroja, B. D. Rainford, L. Menon, S. K. Malik, *J. Phys.: Condens. Matter* **1997**, *9*, 4743.
[133] J. Sakurai, Y. Yamaguchi, S. Nishigori, T. Suzuki, T. Fujita, *J. Magn. Magn. Mater*. **1990**, *90&91*, 422.
[134] Y. Uwatoko, T. Ishii, G. Oomi, S. K. Malik, *Physica B* **1995**, *206&207*, 199.
[135] G. Oomi, T. Kagayama, S. K. Malik, Y. Aoki, H. Sato, Y. Uwatoko, N. Môri, *Rev. High Pressure Sci. Technol*. **1998**, *7*, 382.
[136] D. T. Adroja, B. D. Rainford, A. J. Neville, *Physica B* **1996**, *223&224*, 279.
[137] Y. Uwatoko, M. Kosaka, M. Shirakawa, G. Oomi, N. Môri, T. Kobayashi, H. Tatewaki, K. Shimizu, K. Amaya, *Physica B* **2000**, *284–288*, 1321.
[138] B. D. Rainford, D. T. Adroja, J. M. E. Geers, *Physica B* **1994**, *199&200*, 556.
[139] R. Modler, E. G. Moshopoulou, M. F. Hundley, J. L. Sarrao, J. D. Thompson, Z. Fisk, *Rev. High Pressure Sci*. **1998**, *7*, 598.
[140] P. A. Kotsanidis, Y. K. Yakinthos, W. Schafer, H. Gamari-Seale, *J. Alloys Compd*. **1996**, *235*, 188.
[141] T. Ueda, D. Honda, T. Shiromoto, N. Metoki, F. Honda, K. Kaneko, Y. Haga, T. D. Matsuda, T. Takeuchi, A. Thamizhavel, K. Sugiyama, K. Kindo, R. Settai, Y. Ōnuki, *J. Phys. Soc. Jpn*. **2005**, *74*, 2836.

[142] W. Bażela, J. Leciejewicz, K. Małetka, A. Szytuła, A. Zygmunt, *Acta Phys. Polon. A* **1994**, *85*, 859.
[143] W. Bażela, A. Zygmunt, A. Szytuła, E. Ressouche, J. Leciejewicz, W. Sikora, *J. Alloys Compd*. **1996**, *243*, 106.
[144] R. Asai, A. Thamizhavel, H. Shishido, T. Ueda, Y. Inada, R. Settai, T. C. Kobayashi, Y. Ōnuki, *J. Phys.: Condens. Matter* **2003**, *15*, L463.
[145] T. Ueda, D. Honda, K. Sugiyama, T. Matsuda, N. Metoki, F. Honda, K. Kaneko, Y. Haga, T. Takeuchi, K. Kindo, R. Settai, Y. Ōnuki, *Physica B* **2005**, *359–361*, 133.
[146] Y.-S. Li, B.-L. Du, H.-Y. Wang, X. Zhan, Q.-F. Lu, *J. Atomic Mol. Phys*. **2007**, *24*, 40.
[147] A. Suytuła, M. Kolenda, E. Ressouche, A. Zygmunt, *J. Alloys Compd*. **1997**, *259*, 36.
[148] P. A. Kotsanidis, J. K. Yakinthos, E. Roudaut, H. Gamari-Seale, *J. Magn. Magn. Mater*. **1994**, *131*, 139.
[149] L. Rebelsky, K. Reilly, S. Horn, H. Borges, J. D. Thompson, R. Caspary, *J. Appl. Phys*. **1990**, *67*, 5206.
[150] M. J. Besnus, A. Braghta, N. Hamdaoui, A. Meyer, *J. Magn. Magn. Mater*. **1992**, *104–107*, 1385.
[151] S. K. Malik, D. T. Adroja, S. K. Dhar, R. Vijayaraghavan, B. D. Padalia, *Phys. Rev. B* **1989**, *40*, 2414.
[152] M. Kyogaku, Y. Kitaoka, H. Nakamura, K. Asayama, F. Teshima, T. Takabatake, H. Fujii, Y. Yamaguchi, J. Sakurai, *J. Magn. Magn. Mater*. **1990**, *90&91*, 487.
[153] M. Kasaya, T. Tani, K. Ohoyama, M. Kohgi, Y. Isikawa, *J. Magn. Magn. Mater*. **1992**, *104–107*, 665.
[154] F. Iga, M. Kasaya, H. Suzuki, Y. Okayama, H. Takahashi, N. Mori, *Physica B* **1993**, *186–188*, 419.
[155] M. Kolenda, J. Leciejewicz, N. Stuesser, A. Szytuła, A. Zygmunt, *J. Magn. Magn. Mater*. **1995**, *145*, 85.
[156] D. T. Adroja, B. D. Rainford, *Physica B* **1994**, *194–196*, 363.
[157] H. Kadowaki, T. Ekino, H. Iwasaki, T. Takabatake, H. Fujii, J. Sakurai, *J. Phys. Soc. Jpn*. **1993**, *62*, 4426.
[158] D. T. Adroja, B. D. Rainford, S. K. Malik, *Physica B* **1994**, *194–196*, 169.
[159] B. Cornut, B. Coqblin, *Phys. Rev. B* **1972**, *5*, 4541.
[160] T. Fujita, T. Suzuki, S. Nishigori, T. Takabatake, H. Fujii, J. Sakurai, *J. Magn. Magn. Mater.* **1992**, *108*, 35.
[161] S. Chastin, D. T. Adroja, D. F. Brewer, T. Hargreaves, C. S. McMenamin, B. D. Rainford, A. L. Thomson, *Czech. J. Phys*. **1996**, *46*(Suppl. S5), 2589.
[162] A. K. Bhattacharjee, B. Coqblin, *Phys. Rev. B* **1988**, *38*, 338.
[163] B. C. Sales, D. K. Wohlleben, *Phys. Rev. Lett.* **1975**, *35*, 1240.
[164] J. P. Kuang, H. J. Cui, J. Y. Li, F. M. Yang, H. Nakotte, E. Brück, F. R. de Boer, *J. Magn. Magn. Mater*. **1992**, *104–107*, 1475.
[165] J. Sakurai, D. Huo, D. Kato, T. Kuwai, Y. Isikawa, K. Mori, *Physica B* **2000**, *281&282*, 98.
[166] B. Chevalier, P. Rogl, J. Etourneau, M. J. Besnus, *J. Magn. Magn. Mater*. **1990**, *83*, 303.
[167] T. Sasakawa, K. Shigetoh, D. Hirata, K. Umeo, T. Takabatake, *Physica B* **2005**, *359–361*, 111.
[168] Y. Kawasaki, M. Izumi, Y. Kishimoto, T. Ohno, H. Tou, Y. Inaoka, M. Sera, K. Shigetoh, T. Takabatake, *Phys. Rev. B* **2007**, *75*, 094410.
[169] Y. Kawasaki, T. Tanaka, M. Izumi, Y. Kishimoto, T. Ohno, H. Tou, Y. Inaoka, M. Sera, K. Shigetoh, T. Takabatake, *J. Phys. Chem. Solids* **2007**, *68*, 2195.
[170] P. Morin, D. Gignoux, J. Voiron, A. P. Murani, *Physica B* **1992**, *180&181*, 173.
[171] E. Bauer, *J. Magn. Magn. Mater*. **1992**, *108*, 27.
[172] E. Bauer, E. Gratz, N. Pillmayr, D. Gignouy, D. Schmitt, *J. Magn. Magn. Mater*. **1988**, *76&77*, 131.
[173] Z. Li, Y. Wang, J. Luo, X. Cai, W. Yao, D. Jin, *Physica C* **1991**, *185–189*, 2635.
[174] Y. Wang, J. Luo, D. Jin, X. Cai, *Chin. J. Low Temp. Phys*. **1993**, *15*, 14.
[175] Q. Hu, Z. Xianyu, M. Qiu, X. Yan, Z. Cheng, Q. Zhao, W. Sun, *J. Magn. Magn. Mater*. **1995**, *140–144*, 1225.
[176] E. Bauer, *Adv. Phys.* **1991**, *40*, 417.
[177] H.-M. Hou, D. Jin, Y.-P. Wang, J.-L. Luo, E. Nyeanchi, D. F. Brewer, A. L. Thomson, *Chin. Phys. Lett*. **1998**, *15*, 62.
[178] V. T. Rajan, *Phys. Rev. Lett.* **1983**, *51*, 308.
[179] J. G. Sereni, N. Caroca-Canales, M. Kumar, N. Oeschler, M. Gomez Berisso, C. Geibel, *J. Phys. Conf. Ser.* **2010**, *200*, 012181.
[180] B. Chevalier, E. Gaudin, S. Tencé, B. Malaman, J. Rodriguez Fernandez, G. André, B. Coqblin, *Phys. Rev. B* **2008**, *77*, 014414.
[181] SciFinder Scholar version 2016: http://scifinder.cas.org (entries tracked on April 15th 2016).
[182] R.V. Scolozdra, O.E. Koretskaya, Yu. K. Gorelenko, *Inorg. Mater.* **1984**, *20*, 520.
[183] T. Takabatake, Y. Nakazawa, M. Ishikawa, *Jpn. J. Appl. Phys.* **1987**, *26* (Suppl. 3), 547.
[184] F. G. Aliev, V. V. Moshchalkov, V. V. Kozyrkov, M. K. Zalyalyutdinov, V. V. Pryadun, R. V. Scolozdra, *J. Magn. Magn. Mater.* **1988**, *76–77*, 295.
[185] M. Kurisu, T. Takabatake, H. Fujiwara, *Solid State Commun.* **1988**, *68*, 595.
[186] Y. Yamaguchi, J. Sakurai, F. Teshima, H. Kawanaka, T. Takabatake, H. Fujii, *J. Phys.: Condens. Matter* **1990**, *2*, 5715.
[187] M. Kyogaku, Y. Kitaoka, H. Nakamura, K. Asayama, T. Takabatake, F. Teshima, H. Fujii, *J. Phys. Soc. Jpn.* **1990**, *59*, 1728.
[188] M. Kyogaku, Y. Kitaoka, H. Nakamura, K. Asayama, F. Teshima, T. Takabatake, H. Fujii, Y. Yamaguchi, J. Sakurai, *J. Magn. Magn. Mater.* **1990**, *90*, 487.
[189] T. Takabatake, F. Teshima, H. Fujii, S. Nishigori, T. Suzuki, T. Fujita, Y. Yamaguchi, J. Sakurai, D. Jaccard, *Phys. Rev. B* **1990**, *41*, 9607.
[190] F. G. Aliev, V. V. Moshchalkov, M. K. Zalyalyutdinov, G. I. Pak, R. V. Scolozdra, P. A. Alekseev, V. N. Lazukov, I. P. Sadikov, *Physica B* **1990**, *163*, 358.
[191] M. Kohgi, K. Ohoyama, T. Osakabe, M. Kasaya, T. Takabatake, H. Fujii, *Physica B* **1993**, *186*, 409.
[192] M. Kohgi, K. Ohoyama, T. Osakabe, M. Kasaya, *J. Magn. Magn. Mater.* **1992**, *108*, 187.
[193] T. E. Mason, G. Aeppli, A. P. Ramirez, K. N. Clausen, C. Broholm, N. Stücheli, E. Bucher, T. T. M. Palstra, *Phys. Rev. Lett.* **1992**, *69*, 490.
[194] F. G. Aliev, A. I. Belogorochov, V. V. Moshchalkov, R. V. Scolozdra, M. A. Lopez de la Torre, S. Vieria, R. Villar, *Physica B* **1991**, *171*, 381.
[195] Y. Uwatoko, G. Oomi, T. Takabatake, H. Fujii, *J. Magn. Magn. Mater.* **1992**, *104*, 643.
[196] A. Yanase, H. Harima, *Prog. Theor. Phys. Supplement* **1992**, *108*, 19.
[197] M. Kasaya, *J. Phys. Soc. Jpn.* **1992**, *61*, 3841.
[198] T. Takabatake, M. Nagasawa, H. Fujii, M. Nohara, T. Suzuki, T. Fujita, G. Kido, T. Hiraoka, *J. Magn. Magn. Mater.* **1992**, *108*, 155.
[199] M. Kasaya, T. Tani, F. Iga, T. Kasuya, *J. Magn. Magn. Mater.* **1988**, *76–77*, 278.

[200] T. Takabatake, M. Nagasawa, H. Fujii, G. Kido, K. Sugiyama, K. Senda, K. Kindo, M. Date, *Physica B* **1992**, *177*, 177.
[201] S. Nohara, H. Namatame, A. Fujimori, T. Takabatake, *Physica B* **1993**, *186–188*, 403.
[202] S. Nohara, H. Namatame, A. Fujimori, T. Takabatake, *Phys. Rev. B* **1993**, *47*, 1754.
[203] G. M. Kalvius, A. Kratzer, K. H. Münch, F. E. Wagner, S. Zwirner, H. Kobayashi, T. Takabatake, G. Nakamoto, H. Fujii, S. R. Kreitzmann, R. Kiefl, *Physica B* **1993**, *186–188*, 412.
[204] A. Kratzer, G. M. Kalvius, T. Takabatake, G. Nakamoto, H. Fujii, S. R. Kreitzman, *Europhys. Lett.* **1992**, *19*, 649.
[205] K. Nishimura, I. S. Oliveira, N. J. Stone, P. Richards, S. Ohya, Y. Isikawa, K. Mori, *Physica B* **1993**, *186–188*, 400.
[206] T. Takabatake, G. Nakamoto, T. Yoshino, H. Fujii, K. Izawa, S. Nishigori, H. Goshima, T. Suzuki, T. Fujita, K. Maezawa, T. Hiraoka, Y. Okayama, I. Oguro, A. A. Menovsky, K. Neumaier, A. Brückl, K. Andres, *Physica B* **1996**, *223–224*, 413.
[207] T. Ekino, T. Takabatake, H. Tanaka, H. Fujii, *Phys. Rev. Lett.* **1995**, *75*, 4262.
[208] T. Takabatake, T. Sasakawa, J. Kitagawa, T. Suemitsu, Y. Echizen, K. Umeo, M. Sera, Y. Bando, *Physica B* **2003**, *328*, 53.
[209] J.-Y. So, S.-J. Oh, J.-G. Park, D. T. Adroja, K. A. McEwen, T. Takabatake, *Phys. Rev. B* **2005**, *71*, 214441.
[210] S. K. Malik, D. T. Adroja, *Phys. Rev. B* **1991**, *43*, 6277.
[211] K. Nakamura, Y. Kitaoka, K. Asayama, T. Takabatake, H. Tanaka, H. Fujii, *J. Phys. Soc. Jpn*. **1994**, *63*, 433.
[212] H. Ikeda, K. Miyake, *J. Phys. Soc. Jpn*. **1996**, *65*, 1769.
[213] H. Kumigashira, T. Sato, T. Yokoya, T. Takahashi, S. Yoshii, M. Kasaya, *Phys. Rev. Lett.* **1999**, *82*, 1943.
[214] H. Kumigashira, T. Takahashi, S. Yoshii, M. Kasaya, *Phys. Rev. Lett.* **2001**, *87*, 67206.
[215] T. Ekino, T. Takasaki, T. Suemitsu, T. Takabatake, H. Fujii, *Physica B*, **2002**, *312–313*, 221.
[216] D. T. Adroja, J.-G. Park, K. A. McEwen, K. Shigetoh, T. Sasakawa, T. Takabatake, J.-Y. So, *Physica B* **2006**, *378–380*, 788.
[217] T. Sasakawa, H. Miyaoka, K. Umeo, S. Aoyagi, K. Kato, F. Iga, T. Takabatake, *J. Phys. Soc. Jpn*. **2004**, *73*, 262.
[218] H. Okamura, M. Matsunami, T. Nanba, T. Suemitsu, T. Yoshino, T. Takabatake, Y. Isikawa, H. Harima, *Physica B* **2002**, *312–313*, 218.
[219] M. Matsunami, H. Okamura, T. Nanba, T. Suemitsu, T. Yoshino, T. Takabatake, Y. Isikawa, H. Harima, *J. Phys. Soc. Jpn*. **2002**, *71*, 291.
[220] M. Matsumura, T. Sasakawa, T. Takabatake, S. Tsuji, H. Tou, M. Sera, *J. Phys. Soc. Jpn*. **2003**, *72*, 1030.
[221] T. Sasakawa, K. Mine, K. Shigetoh, T. Takabatake, *J. Phys. Soc. Jpn*. **2005**, *74*, 3329.
[222] K. Shimada, M. Higashiguchi, S.-I. Fujimori, Y. Saitoh, A. Fujimori, H. Namatame, M. Taniguchi, T. Sasakawa, T. Takabatake, *Physica B* **2006**, *383*, 140.
[223] T. Takabatake, H. Tanaka, Y. Bando, H. Fujii, S. Nishigori, T. Suzuki, T. Fujita, G. Kido, *Phys. Rev. B* **1994**, *50*, 623.
[224] T. Ishii, G. Oomi, Y. Uwatoko, T. Takabatake, S. K. Malik, Proceedings of the joint 15 AIRAPT & 33 EHPRG international conference, Warsaw, Poland, september 11–15, **1995**, 764.
[225] T. Takabatake, F. Iga, T. Yoshino, Y. Echizen, K. Katoh, K. Kobayashi, M. Higa, N. Shimizu, Y. Bando, G. Nakamoto, H. Fujii, K. Izawa, T. Suzuki, T. Fujita, M. Sera, M. Hiroi, K. Maezawa, S. Mock, H. v. Löhneysen, A. Brückl, K. Neumaier, K. Andres, *J. Magn. Magn. Mater*. **1998**, *177–181*, 277.
[226] S. K. Malik, L. Menon, V. K. Pecharsky, K. A. Gschneidner, Jr., *Phys. Rev. B* **1997**, *55*, 11471.
[227] J. Moreno, P. Coleman, *Phys. Rev. Lett*. **2000**, *84*, 342.
[228] Y. Kawasaki, Y. Kishimoto, N. Imai, T. Ohno, H. Kubo, S. Yoshii, M. Kasaya, *J. Phys. Soc. Jpn*. **2004**, *73*, 694.
[229] T. Sasakawa, K. Shigetoh, D. Hirata, K. Umeo, T. Takabatake, *Physica B* **2005**, *359–361*, 111.
[230] H. Kobayashi, F. E. Wagner, G. M. Kalvius, T. Takabatake, *Hyperfine Interact.* **1994**, *93*, 1515.
[231] B. Chevalier, A. Wattiaux, L. Fournès, M. Pasturel, *Solid State Sci.* **2004**, *6*, 573.
[232] I. Mischenko, V. Cherepanov, M. Chuev, M. Polikarpov, *Hyperfine Interact.* **2014**, *226*, 299.
[233] R. Pöttgen, *Z. Naturforsch*. **2006**, *61b*, 677.
[234] P. E. Lippens, *Solid State Commun*. **2000**, *113*, 399.
[235] R. Mishra, R. Pöttgen, R.-D. Hoffmann, Th. Fickenscher, M. Eschen, H. Trill, B. D. Mosel, *Z. Naturforsch*. **2002**, *57b*, 1215.
[236] B. Chevalier, J.-L. Bobet, M. Pasturel, E. Bauer, F. Weill, R. Decourt, J. Etourneau, *Chem. Mater*. **2003**, *15*, 2181.
[237] J. Rodriguez Fernandez, S. F. Matar, D. P. Rojas, L. Torralbo-Campo, B. Chevalier, *J. Phys.: Condens. Matter* **2009**, *21*, 305601.
[238] B. Chevalier, J.-L. Bobet, M. L. Kahn, F. Weill, J. Etourneau, *J. Alloys Compd*. **2002**, *334*, 20.
[239] B. Chevalier, E. Gaudin, A. F. Al Alam, S. F. Matar, F. Weill, B. Heying, R. Pöttgen, *Z. Naturforsch*. **2008**, *63b*, 685.
[240] B. Chevalier, J. Sanchez Marcos, J. Rodriguez Fernandez, M. Pasturel, F. Weill, *Phys. Rev. B* **2005**, *71*, 214437.
[241] B. Chevalier, J.-L. Bobet, M. Pasturel, E. Gaudin, J. Etourneau, *J. Alloys Compd*. **2003**, *356–357*, 147.
[242] D. T. Adroja, B. D. Rainford, A. J. Neville, P. Mandal, A. G. M. Jansen, *J. Magn. Magn. Mater*. **1996**, *161*, 157.
[243] Y. Echizen, T. Takabatake, *Physica B* **1999**, *259–261*, 292.
[244] J. S. Flaschin, A. Kratzer, F. J. Burghart, G. M. Kalvius, R. Wäppling, D. R. Noakes, R. Kadono, I. Watanabe, T. Takabatake, K. Kobayashi, G. Nakamoto, H. Fujii, *J. Phys.: Condens. Matter* **1996**, *8*, 6967.
[245] T. Saiki, M. Matsumura, H. Kato, T. Nishioka, T. Sasakawa, T. Takabatake, *J. Magn. Magn. Mater*. **2007**, *310*, e45.
[246] A. Ślebarski, A. Jezierski, S. Mähl, M. Neumann, G. Borstel, *Phys. Rev. B* **1998**, *58*, 4367.
[247] D. T. Adroja, B. D. Rainford, *J. Magn. Magn. Mater*. **1994**, *135*, 333.
[248] E. Lidström, R. Wäppling, S. F. Flaschin, G. M. Kalvius, A. Kratzer, D. T. Adroja, B. D. Rainford, A. Neville, *Hyperfine Interact.* **1997**, *104*, 193.
[249] F. C. Ragel, P. de V. du Plessis, A. M. Strydom, *J. Phys. Chem. Solids* **2010**, *71*, 1694.
[250] B. Andraka, *Phys. Rev. B* **1994**, *49*, 348.
[251] J. S. Kim, E.-W. Scheidt, D. Mixson, B. Andraka, G. R. Stewart, *Phys. Rev. B* **2003**, *67*, 184401.
[252] J.-G. Park, M. Ocko, B. R. Cole, *J. Phys.: Condens. Matter* **1994**, *6*, L781.
[253] J.-G. Park, C. Scott, K. A. McEwen, R. Cywinski, *Physica B* **1997**, *230–232*, 673.
[254] J.-G. Park, M. Očko, K. A. McEwen, *Phys. Rev. B* **1998**, *57*, 13706.

[255] B. Chevalier, P. Rogl, E. K. Hlil, M. H. Tuilier, P. Dordor, J. Etourneau, *Z. Phys. B-Condens. Matter* **1991**, *84*, 205.
[256] M. Kasaya, T. Tani, H. Suzuki, K. Ohoyama, M. Kohgi, *J. Phys. Soc. Jpn*. **1991**, *60*, 2542.
[257] A. Ślebarski, A. Jezierski, S. Mähl, M. Neumann, G. Borstel, *Phys. Rev. B* **1997**, *56*, 7245.
[258] J. Sakurai, R. Kawamura, T. Taniguchi, S. Nishigori, S. Ikeda, H. Goshima, T. Suzuki, T. Fujita, *J. Magn. Magn. Mater*. **1992**, *104–107*, 1415.
[259] S. Nishigori, H. Goshima, T. Suzuki, T. Fujita, G. Nakamoto, H. Tanaka, T. Takabatake, H. Fujii, *J. Phys. Soc. Jpn*. **1996**, *65*, 2614.
[260] D. T. Adroja, B. D. Rainford, A. J. Neville, A. G. M. Jansen, *Physica B* **1996**, *223&224*, 275.
[261] G. M. Kalvius, T. Takabatake, A. Kratzer, R. Wäppling, D. R. Noakes, S. J. Flaschin, F. J. Burghart, R. Kadono, I. Watanabe, A. Brückl, K. Neumaier, K. Andres, K. Kobayashi, G. Nakamoto, H. Fujii, *Hyperfine Interact.* **1997**, *104*, 157.
[262] G. M. Kalvius, S. J. Flaschin, T. Takabatake, A. Kratzer, R. Wäppling, D. R. Noakes, F. J. Burghart, A. Brückl, K. Neumaier, K. Andres, R. Kadono, I. Watanabe, K. Kobayashi, G. Nakamoto, H. Fujii, *Physica B* **1997**, *230–232*, 655.
[263] Y. Bando, Y. Echizen, T. Takabatake, *Physica B* **2000**, *281&282*, 294.
[264] G. M. Kalvius, A. Kratzer, G. Grosse, D. R. Noakes, R. Wäppling, H. v. Löhneysen, T. Takabatake, Y. Echizen, *Physica B* **2000**, *289–290*, 256.
[265] B. Janoušová, V. Sechovský, A. H. Lacerda, T. Komatsubara, *J. Magn. Magn. Mater*. **2004**, *272–276*, e117.
[266] D. T. Adroja, B. D. Rainford, *Physica B* **1994**, *199&200*, 498.
[267] D. T. Adroja, B. D. Rainford, J. M. de Teresa, A. del Moral, M. R. Ibarra, K. S. Knight, *Phys. Rev. B* **1995**, *52*, 12790.
[268] T. J. Sato, H. Kadowaki, H. Yoshizawa, T. Takabatake, H. Fujii, Y. Isikawa, *J. Phys.: Condens. Matter* **1996**, *8*, 7127.
[269] T. J. Sato, H. Kadowaki, H. Yoshizawa, G. Nakamoto, T. Ekino, T. Takabatake, H. Fujii, L. P. Regnault, Y. Isikawa, *Physica B* **1996**, *223&224*, 432.
[270] M. Sera, N. Kobayashi, T. Yoshino, K. Kobayashi, T. Takabatake, G. Nakamoto, H. Fujii, *Phys. Rev. B* **1997**, *55*, 6421.
[271] D. T. Adroja, Y. Echizen, T. Takabatake, Y. Matsumoto, T. Suzuki, T. Fujita, B. D. Rainford, *J. Phys.: Condens. Matter* **1999**, *11*, 543.
[272] T. Takabatake, Y. Echizen, T. Yoshino, K. Kobayashi, G. Nakamoto, H. Fujii, M. Sera, *Phys. Rev. B* **1999**, *59*, 13878.
[273] K. Kumagai, Y. Furukawa, K. Ooi, B. Rainford, A. Yakubovskii, *Physica B* **1999**, *259–261*, 294.
[274] D. T. Adroja, B. D. Rainford, M. Houshiar, *J. Alloys Compd*. **1998**, *268*, 1.
[275] A. Ślebarski, M. B. Maple, R. E. Baumbach, T. A. Sayles, *Phys. Rev. B* **2008**, *77*, 245133.
[276] A. Ślebarski, M. Fijałkowski, *Physica B* **2009**, *404*, 2969.
[277] A. Ślebarski, M. B. Maple, M. Fijałkowski, J. Goraus, *J. Phys.: Condens. Matter* **2010**, *22*, 165601.
[278] A. Ślebarski, A. Jezierski, A. Zygmunt, S. Mähl, M. Neumann, G. Borstel, *Phys. Rev. B* **1996**, *54*, 13551.
[279] A. Brückl, K. Neumaier, Ch. Probst, K. Andres, S. J. Flaschin, A. Kratzer, G. M. Kalvius, T. Takabatake, *Physica B* **1997**, *240*, 199.
[280] A. Kratzer, *Appl. Magn. Res*. **1997**, *13*, 137.
[281] A. Schröder, G. Aeppli, T. E. Mason, E. Bucher, *Physica B* **1997**, *234–236*, 861.
[282] Y. Echizen, K. Uemo, S. Hamashima, T. Fujita, T. Takabatake, N. Kobayashi, I. Oguro, *Solid State Commun*. **2000**, *115*, 587.
[283] A. Ślebarski, M. Radłowska, A. Zygmunt, A. Jezierski, *Phys. Rev. B* **2002**, *65*, 205110.
[284] Y. Bando, T. Takabatake, H. Fujii, G. Kido, *Physica B* **1995**, *206&207*, 822.
[285] A. Ślebarski, M. Fijałkowski, *Solid State Phen*. **2011**, *170*, 51.
[286] L. Menon, F. E. Kayzel, A. de Visser, S. K. Malik, *Phys. Rev. B* **1998**, *58*, 85.
[287] M. Eilers-Rethwisch, O. Niehaus, O. Janka, *Z. Anorg. Allg. Chem*. **2014**, *640*, 153.
[288] H. H. Cho, W. H. Lee, Y. Y. Chen, *Solid State Commun*. **2004**, *130*, 821.
[289] F. C. Ragel, P. de V. du Plessis, A. M. Strydom, *J. Magn. Magn. Mater*. **2007**, *310*, 365.
[290] J. F. Riecken, W. Hermes, B. Chevalier, R.-D. Hoffmann, F. M. Schappacher, R. Pöttgen, *Z. Anorg. Allg. Chem*. **2007**, *633*, 1094.
[291] Ch. D. Routsi, J. K. Yakinthos, H. Gamari-Seale, *J. Magn. Magn. Mater*. **1992**, *117*, 79.
[292] O. Niehaus, P. M. Abdala, R. Pöttgen, *Z. Naturforsch*. **2015**, *70b*, 253.
[293] O. Niehaus, P. M. Abdala, R. S. Touzani, B. P. T. Fokwa, R. Pöttgen, *Solid State Sci*. **2015**, *40*, 36.
[294] A. Ślebarski, T. Zawada, J. Spałek, A. Jezierski, *Phys. Rev. B* **2004**, *70*, 235112.
[295] A. Ślebarski, J. Spałek, *Phys. Rev. Lett*. **2005**, *95*, 046402.
[296] A. Ślebarski, T. Zawada, J. Spałek, *Physica B* **2005**, *359–361*, 118.
[297] A. Ślebarski, *J. Low Temp. Phys*. **2007**, *147*, 147.
[298] A. Ślebarski, J. Spałek, *Acta Phys. Polon. A* **2007**, *111*, 487.
[299] A. Ślebarski, J. Spałek, *Phil. Mag*. **2009**, *89*, 1845.
[300] J. Goraus, A. Ślebarski, *Phys. Stat. Solidi B* **2013**, *250*, 533.
[301] A. del Moral, C. de la Fuente, *J. Magn. Magn. Mater*. **2010**, *322*, 1143.
[302] A. Fraile, A. Del Moral, C. de la Fuente, *J. Magn. Magn. Mater*. **2007**, *310*, e15.
[303] C. de la Fuente, A. Del Moral, D. T. Adroja, A. Fraile, J. I. Arnaudas, *J. Magn. Magn. Mater*. **2010**, *322*, 1059.